

# Antisymmetrized molecular dynamics and its applications to cluster phenomena

Yoshiko KANADA-EN'YO<sup>1</sup>, Masaaki KIMURA<sup>2</sup>, and Akira ONO<sup>3</sup>

<sup>1</sup>*Department of Physics, Kyoto University, Kyoto 606-8502, Japan*

<sup>2</sup>*Creative Research Initiative "Sousei," Hokkaido University, Sapporo 001-0021, Japan*

<sup>3</sup>*Department of Physics, Tohoku University, Sendai 980-8578, Japan*

Structure and reaction studies with a method of antisymmetrized molecular dynamics (AMD) were reviewed. Applications of time-independent and time-dependent versions of the AMD were described. In applications of time-independent AMD to nuclear structure studies, structures of neutron-rich nuclei such as Be, C, Ne, and Mg isotopes were described focusing on cluster aspects. Important roles of valence neutrons were discussed. The results suggested a variety of cluster structures appear also in unstable nuclei as well as in stable nuclei. Deformation and cluster phenomena in  $Z \sim N$  nuclei in  $p$ - and  $sd$ - shell regions were also discussed. Applications of time-dependent AMD contain various topics such as fragmentation in heavy-ion collisions as well as nuclear responses. The AMD calculations successfully describe multifragmentation which is one of the remarkable phenomena in heavy-ion collisions. The approach is able to link reactions and nuclear matter properties. The studies suggested the important balance between single-particle motions and correlations to form clusters and fragments.

## Contents

<b>1. Introduction</b>	<b>2</b>
<b>2. Antisymmetrized molecular dynamics (AMD)</b>	<b>3</b>
2.1. Basic formulation of AMD . . . . .	4
2.2. Basis AMD and its Extensions in applications . . . . .	7
2.3. Branching in time evolution . . . . .	9
<b>3. Applications of time-independent AMD method to nuclear structure</b>	<b>11</b>
3.1. Molecular structures in Be and Ne isotopes . . . . .	11
3.2. Three-body cluster states in $^{12}\text{C}$ , $^{11}\text{B}$ , and $^{14}\text{C}$ . . . . .	14
3.3. Spectroscopy and exotic phenomena in the island of inversion . . . . .	18
3.4. Superdeformation in $sd$ -shell nuclei . . . . .	23
3.5. Decoupling between Proton and neutron deformations . . . . .	27
<b>4. Applications of time-dependent AMD method to nuclear response and reaction</b>	<b>29</b>
4.1. Dipole resonances . . . . .	30
4.2. Radial oscillations . . . . .	31
4.3. Multifragmentation in expanding systems . . . . .	33
4.4. Fragmentation in collisions of light nuclei . . . . .	36
4.5. Statistical properties of excited systems . . . . .	37
4.6. Symmetry energy effects in heavy-ion collisions . . . . .	40

## 5. Summary and perspective

42

### §1. Introduction

A nucleus is a finite quantum many-body system consisting of protons and neutrons interacting via nuclear forces. Its ground state has shell structure, in which nucleons move almost independently in an averaged field (mean field) analogously to an atomic system. The shell structure and excitation modes associated with single-particle and collective motions are important facets of nuclear system.

On the other hand, in nuclear systems, one may also find unique characters different from atomic systems. One of the important differences is that a nucleus is a self-bound system formed by attractive nuclear forces. Because of the attraction, spatial correlations among nucleons can be rather strong, and therefore, assembling and disassembling of nucleons occur in various ways. Furthermore, the saturation property of nuclear system, where binding energy per nucleon and central density are almost constant independently to the mass number, implies that assembling and disassembling of nucleons can take place with a small excitation energy. As well known, this characteristic of nuclear system manifests itself as cluster structures in which a nucleus is divided into several subunits (clusters) and nucleons are confined within each cluster. The important roles of assembling and disassembling of nucleons continue to higher excitation energies as in intermediate-energy heavy-ion collisions where a lot of clusters and fragment nuclei are produced from a hot source whose excitation energy is typically comparable to the binding energy of a nucleus.

In spite of importance of cluster aspect in nuclear systems, usual mean-field approaches often fail to describe those cluster phenomena because they take into account insufficiently many-body correlations, which are essential in cluster formation. The theoretical method of antisymmetrized molecular dynamics (AMD)<sup>1), 2), 3), 4), 5), 6), 7)</sup> has been proposed in studies of heavy-ion collisions. AMD describes nuclear many-body systems by antisymmetrized products of Gaussian wave packets of nucleons and incorporates quantum effects and nucleon-nucleon collisions. It has described fragment formation in heavy-ion collisions successfully. AMD has been proved to be a powerful tool also for nuclear structure study. All centers of the Gaussian packets are independently treated as variational parameters in the AMD framework, and it is possible to describe various cluster structure wave functions as well as independent-particle motion in a mean field without *a priori* assumption. Thus, AMD has been applied to investigate various phenomena in nuclear structure and reactions.

In the early days, AMD studies were limited to light systems. This is because computational cost increases rapidly in proportion to  $A^{4\sim 6}$  ( $A$  is the mass number) due to the non-orthogonality of single-particle wave functions. However, AMD calculations have developed remarkably toward various nuclear systems owing to the rapid progress of computational facilities. For instance, it enabled the reaction studies by AMD up to Au+Au collisions ( $A \sim 400$ )<sup>8)</sup> the structure studies up to *pf*-shell nuclei ( $A \sim 40$ )<sup>9)</sup> and variational calculation after the angular momentum projection that covers up to very high excitation energy.<sup>10)</sup> Further high-performance computing will extend the subjects of AMD studies and enable more sophisticated AMD

calculations.

AMD studies have revealed that cluster phenomena emerge widely in various nuclear systems. Many exotic and novel features of clustering have been discovered and the concept of the clustering has been renewed and extending now. Today, it is well established that clustering is an essential aspect of nuclear many-body systems as well as the mean-field aspect. Coexistence of cluster and mean-field aspects brings out rich phenomena to nuclear many-body systems as functions of excitation energy and isospin degrees of freedom (Fig. 1). As the excitation energy increases, one may see transitions from mean-field to cluster structures. In deeply bound systems such as low-lying states of stable nuclei, mean-field effects are rather strong. However, even if a nucleus has a shell-model-like structure in its ground state, developed cluster structures appear in excited states near the corresponding cluster-decay threshold energy (so-called Ikeda's threshold rule<sup>11</sup>). Above the threshold energy, further remarkable cluster phenomena such as alpha decays, molecular resonances, and fission etc. are known. The coexistence and competition between the clustering and mean field have been studied by AMD in a unified way within a single theoretical framework. When the excitation energy increases further, nuclear systems may enter the region of nuclear liquid-gas phase transition. AMD studies have confirmed the phase transition by obtaining caloric curves for equilibrium systems. The link between the phase transition and copious fragment formation in heavy-ion collisions is now clearer with the unified description by time-dependent AMD. Another important degree of freedom in nuclear systems is the isospin asymmetry, i.e., neutron (proton) excess, which is one of the major directions in recent nuclear physics. In the neutron-rich and proton-rich domains, the saturation law of energy and density is broken. Because of the unbalanced proton-neutron ratio, we may encounter many novel cluster phenomena in isospin asymmetric systems. Indeed, such exotic clustering phenomena as cluster structures in neutron-rich Be isotopes and isospin fractionation/distillation at liquid-gas separation in fragmentation reactions have been investigated with AMD.

In this paper, we review the AMD approach and its applications to nuclear structures and reactions. In the next section, the formulation of AMD is described. Applications of the time-independent version of AMD to static problems of nuclear structures are explained in §3, and those of the time-dependent version to dynamical phenomena such as nuclear responses and nuclear reactions are described in §4. Finally, a summary and perspectives are given in §5.

## §2. Antisymmetrized molecular dynamics (AMD)

As mentioned above, cluster aspect is one of the essential features of nuclear systems as well as mean-field aspect. Originating in coexistence of two kinds of nature, cluster and mean-field aspects, a variety of phenomena arise in nuclear many-body systems. To investigate rich phenomena concerning cluster aspects such as cluster structures and multifragmentations, a theoretical framework that can describe both the cluster and mean-field features is required. The AMD method has been proved to be one of the powerful approaches in description of those features. In this section,

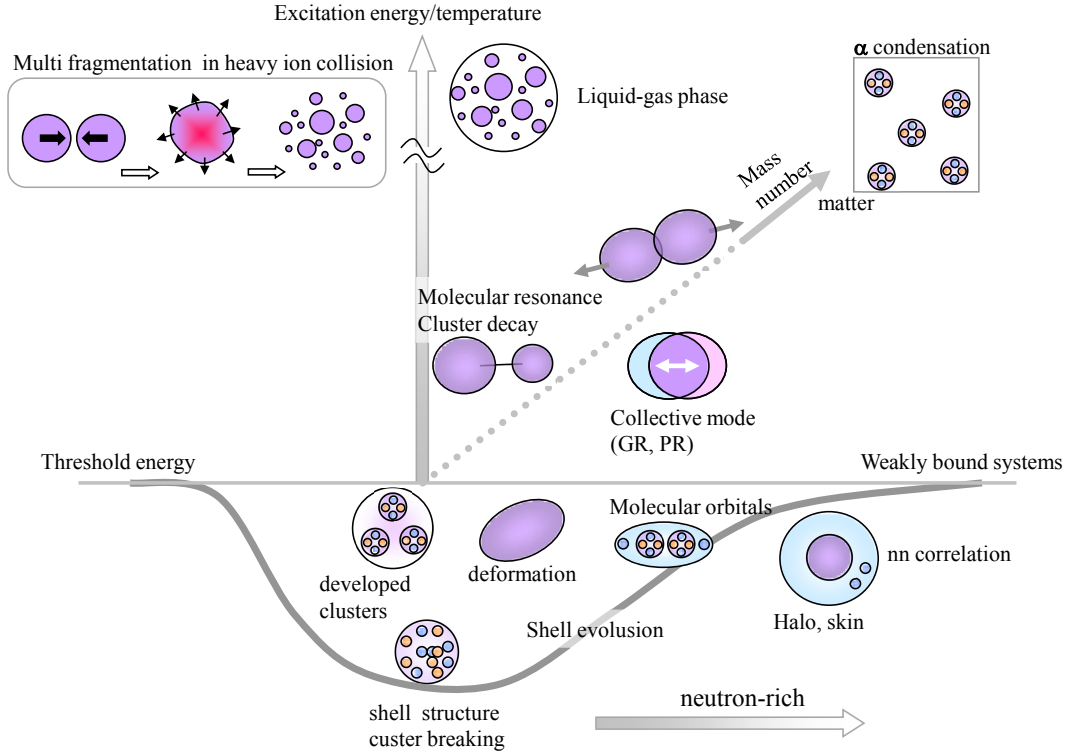


Fig. 1. Schematic figure for rich phenomena in nuclear systems.

we briefly review formulation of AMD. After describing basic formalism of AMD, we explain extended methods of AMD which have been applied to nuclear structure and nuclear reaction studies. For detailed formulation of the AMD method, the reader is referred to Refs. 4), 5), 6), 7).

## 2.1. Basic formulation of AMD

### 2.1.1. AMD wave function

In the AMD framework, an basis wave function for an  $A$ -nucleon system is expressed by a Slater determinant of Gaussian wave packets;

$$\Phi_{\text{AMD}}(Z) = \frac{1}{\sqrt{A!}} \mathcal{A}\{\varphi_1, \varphi_2, \dots, \varphi_A\}, \quad (2.1)$$

where the  $i$ th single-particle wave function is written by a product of spatial ( $\phi$ ), intrinsic spin ( $\chi$ ), and isospin ( $\tau$ ) wave functions as follows.

$$\varphi_i = \phi_{\mathbf{z}_i} \chi_i \tau_i, \quad (2.2)$$

$$\phi_{\mathbf{z}_i}(\mathbf{r}_j) \propto \exp\left(-\nu\left(\mathbf{r}_j - \frac{\mathbf{z}_i}{\sqrt{\nu}}\right)^2\right), \quad (2.3)$$

$$\chi_i = \left(\frac{1}{2} + \xi_i\right)\chi_\uparrow + \left(\frac{1}{2} - \xi_i\right)\chi_\downarrow. \quad (2.4)$$

The spatial part  $\phi_{\mathbf{Z}_i}$  of the  $i$ th single-particle wave function is represented by a complex variational parameter  $Z_{i\sigma}$  with  $\sigma = x, y, z$  which indicates the center of the Gaussian wave packet. The spin part  $\chi_i$  is parametrized by a complex number parameter,  $\xi_i$ . The isospin function  $\tau_i$  is fixed to be up (proton) or down (neutron). The width parameter  $\nu$  takes a common value for all nucleons. It is chosen to be an optimum value for the studied system. Accordingly, an AMD wave function is expressed by a set of variational parameters,  $Z \equiv \{\mathbf{Z}_1, \mathbf{Z}_2, \dots, \mathbf{Z}_A, \xi_1, \xi_2, \dots, \xi_A\}$ . These parameters indicate centers of localized Gaussians and spin orientations, which are treated independently for all nucleons. That is to say, a system written by a single AMD wave function is specified by the configuration of single-nucleon wave packets in the phase space and their spin orientations. In the simplest version of AMD, the spin part  $\chi_i$  is sometimes fixed to be up or down, and only parameters  $\mathbf{Z}_1, \mathbf{Z}_2, \dots, \mathbf{Z}_A$  for Gaussian centers are treated as variational parameters. In time-dependent AMD, intrinsic spin orientations are usually fixed. In the case of fixed spins, we redefine  $Z \equiv \{\mathbf{Z}_1, \mathbf{Z}_2, \dots, \mathbf{Z}_A\}$  by omitting the spin labels  $\xi_i$ .

In the AMD wave function, all single nucleons are treated independently as localized Gaussians. Although any constituent clusters are not assumed *a priori*, multi-cluster structures can be described by grouping of single-nucleon Gaussian wave packets in the spatial configuration. On the other hand, if all the Gaussian centers gather around a certain position, the AMD wave function becomes equivalent to a harmonic oscillator shell-model wave function around the position due to the effect of antisymmetrization. Thus, the model space of AMD can describe both cluster and mean-field features with assembling and disassembling of Gaussian wave packets. If a system favors a specific cluster channel, such a cluster structure will be automatically obtained in energy variation or in dynamics.

The AMD wave function is quite similar to a wave function of fermionic molecular dynamics (FMD)<sup>12),13)</sup> where more generalized wave functions are adopted. In applications of AMD to nuclear structure and reaction studies, the description has been improved by superposing many AMD wave functions or by introducing stochastic processes rather than by choosing more general single-particle wave functions.

### 2.1.2. Equation of motion

In the time-dependent versions of the AMD method which have been applied to dynamics of nuclear systems, the time evolution of the variational parameters  $Z$  are determined by the time-dependent variational principle. The equation of motion for  $Z$  derived from the time-dependent variational principle is

$$i\hbar \sum_{j\rho} C_{i\sigma,j\rho} \frac{dZ_{j\rho}}{dt} = \frac{\partial \mathcal{H}}{\partial Z_{i\sigma}^*}, \quad (2.5)$$

where  $\sigma, \rho = x, y, z$  are the labels for the components of  $\mathbf{Z}_i$  ( $i = 1, 2, \dots, A$ ). When the spin wave function is a variable, it may be regarded as the fourth component

$Z_{i4} = \xi_i$ . The expectation value of the Hamiltonian  $\hat{H}$  is given by

$$\mathcal{H}(Z, Z^*) = \frac{\langle \Phi_{\text{AMD}}(Z) | \hat{H} | \Phi_{\text{AMD}}(Z) \rangle}{\langle \Phi_{\text{AMD}}(Z) | \Phi_{\text{AMD}}(Z) \rangle}. \quad (2.6)$$

A positive definite Hermitian matrix

$$C_{i\sigma, j\rho} \equiv \frac{\partial^2}{\partial Z_{i\sigma}^* \partial Z_{j\rho}} \ln \langle \Phi_{\text{AMD}}(Z) | \Phi_{\text{AMD}}(Z) \rangle \quad (2.7)$$

appears in the equation of motion, suggesting that the variables  $Z$  are not canonical coordinates.

### 2.1.3. Energy variation

To get an optimum solution for the energy minimum state, the energy variation is performed. Namely, the variational parameters  $Z$  are optimized to minimize the expectation value of the Hamiltonian in the AMD model space. We introduce the following frictional cooling equation,

$$i\hbar \sum_{j\rho} C_{i\sigma, j\rho} \frac{dZ_{j\rho}}{dt} = (\lambda + i\mu) \frac{\partial \mathcal{H}}{\partial Z_{i\sigma}^*}. \quad (2.8)$$

The parameter  $\lambda$  is an arbitrary real number and  $\mu$  is an arbitrary negative real number. It is easily proved that the energy of the system decreases as time develops due to the frictional term  $i\mu$ . In the energy variation, the matrix  $C_{i\sigma, j\rho}$  can be replaced with  $\delta_{ij}\delta_{\sigma\rho}$  and then, the frictional cooling method with  $\lambda = 0$  becomes equivalent to the steepest decent method. In both cases of  $C_{i\sigma, j\rho}$ , we obtain the optimum set of parameters  $Z$  that gives the AMD wave function for the minimum energy state in the model space after enough cooling time (iteration steps).

### 2.1.4. Hamiltonian

The Hamiltonian for an  $A$ -nucleon system consists of the kinetic energy, the nuclear and Coulomb force terms,

$$\hat{H} = \sum_i \hat{t}_i + \sum_{i,j} \hat{v}_{ij} + \sum_{i,j} \hat{v}_{ij}^{\text{coulomb}} - \hat{T}_g. \quad (2.9)$$

Here  $\hat{t}_i$  is the kinetic energy. The energy of the center-of-mass motion  $\hat{T}_g$  is subtracted exactly because the total wave function can be separated into the internal wave function and the center-of-mass wave function. In applications to heavy ion collisions, spurious kinetic energy of the zero-point oscillation of fragment mass centers is also subtracted from the Hamiltonian. For the effective two-body nuclear force  $\hat{v}_{ij}$ , finite-range forces such as Volkov<sup>14)</sup> forces supplemented by G3RS form spin-orbit forces,<sup>15)</sup> Gogny<sup>16),17)</sup> forces, and Skyrme<sup>18),19)</sup> forces are used. Finite-range two-body forces with zero-range three-body forces such as the modified Volkov forces<sup>20)</sup> are also used. The Coulomb force  $\hat{v}_{ij}^{\text{coulomb}}$  is approximated by a sum of seven Gaussians.

These effective forces are phenomenological ones constructed to describe low-energy properties of nuclear structure. In heavy-ion reaction, residual interactions contribute to nucleon-nucleon collisions which are incorporated by stochastic collision process in the AMD framework as explained later.

## 2.2. Basis AMD and its Extensions in applications

In the early stage of AMD studies, simple versions of the AMD method have been applied to reaction and structure studies,<sup>(1),2),3)</sup> and later, the AMD method has been developed to many extended versions (Refs. 4), 6), 7) and references therein). In this section, we explain the formulation of the basic AMD method and some advanced versions for structure study and those for reaction study.

An basis AMD wave function is given by a single Slater determinant. Generally, many-body wave functions for quantum systems should be expressed by a superposition of many Slater determinants. Restriction of the model space within a single Slater determinant is the limit of a mean-field approximation. To incorporate beyond-mean-field effects, superposition of Slater determinants is essential. Firstly, in structure study, parity and angular-momentum projections, which are done by superposition of Slater determinants, are essential to describe properties of energy-eigen states. In second, superposition of Slater determinants is significant to improve wave functions by taking into account quantum fluctuation around a mean-field, many-body correlations, and spin-parity projections. It is also necessary to describe excited states orthogonal to lower states.

In applications of the AMD method to structure study, the projections and superposition of AMD wave functions are practically performed. In applications to heavy-ion reactions, however, emergence of multiple reaction channels is introduced by stochastic branching processes, neglecting quantum interference between different channels each of which is described by an AMD wave function.

### 2.2.1. Projections and superposition of AMD wave functions

The parity-projected AMD wave function is given as

$$|\Phi_{\text{AMD}}^{\pm}\rangle \equiv P^{\pm}|\Phi_{\text{AMD}}(Z)\rangle = \frac{1 \pm \hat{P}_r}{2}|\Phi_{\text{AMD}}(Z)\rangle, \quad (2.10)$$

where  $P^{\pm} = 1 \pm \hat{P}_r$  is the parity projection operator. The angular-momentum projected AMD wave function is written as

$$|\Phi_{MK}^J\rangle = P_{MK}^J|\Phi_{\text{AMD}}(Z)\rangle = \int d\Omega D_{MK}^{J*}(\Omega)\hat{R}(\Omega)|\Phi_{\text{AMD}}(Z)\rangle. \quad (2.11)$$

Here  $D_{MK}^J(\Omega)$  is the Wigner's  $D$  function and  $\hat{R}(\Omega)$  is a rotation operator with respect to Euler angle  $\Omega$ . As clearly shown, the angular-momentum projected state is expressed by a linear combination of wave functions rotated from the intrinsic AMD wave function  $\Phi_{\text{AMD}}(Z)$  with the weight function,  $D_{MK}^{J*}$ . The matrix element of a tensor operator  $\hat{T}_q^k$ , where  $k$  is the rank and  $q$  is the  $z$ -component, can be calculated to be

$$\begin{aligned} \langle P_{MK}^J\Phi_{\text{AMD}}(Z)|\hat{T}_q^k|P_{M'K'}^{J'}\Phi_{\text{AMD}}(Z')\rangle &= \frac{8\pi^2}{2J+1}\langle J'M'kq|JM\rangle \\ &\times \sum_{\mu\nu} \langle J'\mu k\nu|JK\rangle \int d\Omega D_{\mu K'}^{J'*}(\Omega)\langle\Phi_{\text{AMD}}(Z)|\hat{T}_\nu^k\hat{R}(\Omega)|\Phi_{\text{AMD}}(Z')\rangle. \end{aligned} \quad (2.12)$$

In practical calculations, the integrations with respect to  $\Omega$  is performed by numerical integration on grid points of angles  $\Omega = (\theta_1, \theta_2, \theta_3)$ . In calculations of expectation values for observable operators such as Hamiltonian, radii, moments, and transitions, AMD wave functions are projected to parity and angular-momentum eigenstates. In the usual AMD calculations for structure study, the parity projection is done before energy variation while the angular-momentum projection is performed after the energy variation, i.e., variation before projection (VBP).

Superposition of independent AMD wave functions is useful to improve wave functions and it is essential in description of excited states to satisfy orthogonality between energy levels. Let us consider superposition of independent AMD wave functions  $\Phi_{\text{AMD}}(Z^{(k)})$  ( $k = 1, \dots, k_{\text{max}}$ ) ( $k_{\text{max}}$  is the number of adopted basis AMD wave functions). Superposed wave functions for  $J^\pm$  states is written as

$$|\Phi_n^{J^\pm}\rangle = \sum_{kK} c_{n,kJK} |P_{MK}^{J^\pm} \Phi_{\text{AMD}}(Z^{(k)})\rangle, \quad (2.13)$$

where  $P_{MK}^{J^\pm} \equiv P_{MK}^J P^\pm$ . Here the values for the coefficients  $c_{n,kJK}$  are determined by the variational principle,

$$\delta \{ \langle \Phi_n^{J^\pm} | \hat{H} | \Phi_n^{J^\pm} \rangle - \epsilon_n \langle \Phi_n^{J^\pm} | \Phi_n^{J^\pm} \rangle \} = 0, \quad (2.14)$$

which is equivalent to diagonalization of the norm and the Hamiltonian matrices and leads to the Hill-Wheeler equations. The  $K$  sum in Eq. (2.13) stands for the  $K$ -mixing.

To adopt efficient AMD wave functions as basis wave functions for the superposition, constraint methods, which are often used in a generator coordinates method (GCM),<sup>21),22),23),24)</sup> or stochastic variational methods<sup>25)</sup> are applied in the AMD framework. Here we consider a constraint  $\langle \hat{g} \rangle = \bar{g}$ . By changing the constraint value as  $\bar{g} = \bar{g}_1, \bar{g}_2, \dots, \bar{g}_{k_{\text{max}}}$ , the minimum energy state  $\Phi_{\text{AMD}}^\pm(\bar{g})$  in the AMD model space is obtained for each constraint value by the constraint energy variation after parity projection. Then the obtained wave functions  $\Phi_{\text{AMD}}^\pm(\bar{g}_k)$  ( $k = 1, \dots, k_{\text{max}}$ ) are superposed, and coefficients are determined by the diagonalization. This method corresponds to a GCM calculation for a generator coordinate  $\bar{g}$  when an enough number of the basis wave functions for different values  $\bar{g}_k$  are taken into account. This method (called AMD+GCM) is useful, in particular, for study of excited states. For the constraints, the nuclear quadrupole deformation parameters are often used.<sup>22),23),24)</sup> In the AMD+GCM method, variation is done before the angular-momentum projection.

It is also efficient to perform variation after the angular-momentum projection as well as the parity projection, especially, for study of excited states. Namely, the energy expectation value for a parity and angular-momentum projected AMD wave function,

$$\mathcal{H} = \frac{\langle P_{MK}^{J^\pm} \Phi_{\text{AMD}}(Z) | \hat{H} | P_{MK}^{J^\pm} \Phi_{\text{AMD}}(Z) \rangle}{\langle P_{MK}^{J^\pm} \Phi_{\text{AMD}}(Z) | P_{MK}^{J^\pm} \Phi_{\text{AMD}}(Z) \rangle}, \quad (2.15)$$

is minimized with respect to the variational parameters  $Z$  by using the frictional cooling method. Firstly, for a given spin and a parity  $J^\pm$ , the wave function for



the lowest  $J^\pm$  state is obtained by the energy variation. Then, a wave function for a higher state ( $J_n^\pm$ ) is provided by varying  $Z$  to minimize the energy for the component of an AMD wave function orthogonal to the lower states ( $J_1^\pm, \dots, J_{n-1}^\pm$ ) which are already obtained. In the present paper, we call the variation after spin-parity projection ‘‘VAP’’.<sup>10)</sup>

### 2.2.2. Extensions for single-particle wave functions

In a basis AMD wave function, a single-particle wave function is written by a spherical Gaussian. In extended versions of AMD, a single-particle wave function is written by a deformed Gaussian or superposition of different-range Gaussians to improve single-particle wave functions.<sup>22),23),26),27)</sup> In the method of deformed-basis AMD,<sup>22),23)</sup> triaxially deformed Gaussians are employed as single-particle wave packets instead of spherical ones,

$$\phi_{\mathbf{z}_i}(\mathbf{r}_j) \propto \exp\left\{-\sum_{\sigma=x,y,z} \nu_\sigma \left(r_{j\sigma} - \frac{Z_{i\sigma}}{\sqrt{\nu_\sigma}}\right)^2\right\}, \quad (2.16)$$

where the width parameters,  $\nu_x$ ,  $\nu_y$  and  $\nu_z$ , take different values for each direction. They are determined in the energy variation to optimize energy of a system. By using this deformed basis, it is possible to successfully describe coexistence (or mixing) of cluster and deformed mean-field structures, which are essential especially in heavy systems.

Superposing different range Gaussians is another method to improve single-particle wave functions of an AMD wave function as is done in the FMD method.<sup>26),27)</sup>

Instead of adopting deformed or superposing Gaussians, a method of stochastic branching on wave packets is used to describe the diffusion and deformation of single-particle motions in the time-dependent version of AMD for nuclear reaction calculations<sup>8),28),29)</sup> as explained in the next subsection.

### 2.3. Branching in time evolution

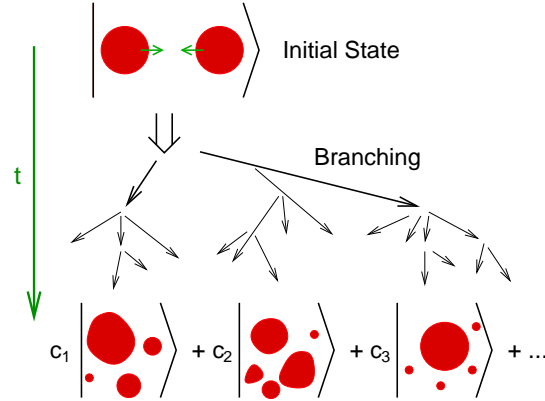


Fig. 2. A schematic picture of the quantum branching processes for multichannel reactions.

The description of dynamics of excited nuclear many-body systems, such as in heavy-ion collisions, is a highly quantum-mechanical many-body problem. If the

many-body time-dependent Schrödinger equation is solved for an initial state which may be roughly approximated by a single Slater determinant, the intermediate and final states will be a very complicated states containing a huge number of reaction channels corresponding to different fragmentation configurations, as illustrated in Fig. 2. The AMD model for reactions respects the existence of channels, while it neglects some of the interference among them. Namely, the total many-body wave function  $|\Psi(t)\rangle$  is approximated by a mixed state

$$|\Psi(t)\rangle\langle\Psi(t)| \approx \int \frac{|\Phi(Z)\rangle\langle\Phi(Z)|}{\langle\Phi(Z)|\Phi(Z)\rangle} w(Z, t) dZ, \quad (2.17)$$

where each component is represented by an AMD wave function  $|\Phi(Z)\rangle$  with a time-dependent weight  $w(Z, t)$ .

Interference between quite different components is not of practical importance because the matrix elements are negligible for the Hamiltonian and other operators of our usual interest. Furthermore, when we adopt mean field approximation in some way, we need to take care of the spurious nonlinearity introduced by the approximation. A many-body state composed of different reaction channels cannot be described by a single mean field. Our strategy is to suitably decomposed the state in such a way that the mean field approximation is valid in each component.

Let us consider the motion of a nucleon in the system, ignoring the Pauli principle for the moment. In mean field approximation, the one-body density matrix is given by a pure single-particle wave function  $\hat{\rho}(t) = |\psi(t)\rangle\langle\psi(t)|$  at any time. Under the mean field, the phase space distribution will spread in some directions and may shrink in other directions. In contrast, in the real time evolution, the condition  $\hat{\rho}(t)^2 = \hat{\rho}(t)$  should no longer hold due to many-body correlations. Namely, decoherence should occur on the single-particle state so that it turns into a mixed state. In the AMD approach, decoherence is taken into account by splitting the wave packet in such a way that the spreading of the distribution in the mean field is respected while the shrinking is discarded. By the decoherence of the single-particle states, the decomposition (or branching) of the many-body state is induced naturally. This approach of using compact wave packets is advantageous for the case with many fragmentation channels because it is free from spurious coupling of different fragmentation channels.

Instead of directly considering the weight function  $w(Z, t)$  in Eq. (2.17), we solve a stochastic equation of motion for the wave packet centroids  $Z$ , which may be symbolically written as

$$\frac{d}{dt}\mathbf{Z}_i = \{\mathbf{Z}_i, \mathcal{H}\}_{\text{PB}} + (\text{NN coll}) + \Delta\mathbf{Z}_i(t) + \mu(\mathbf{Z}_i, \mathcal{H}'). \quad (2.18)$$

The first term  $\{\mathbf{Z}_i, \mathcal{H}\}_{\text{PB}}$  is that in the deterministic equation of motion [Eq. (2.5)] derived from the time-dependent variational principle.

The second term represents the effect of stochastic two-nucleon collisions, where a parametrization of the energy-dependent in-medium cross section is adopted. The collisions are performed with the ‘‘physical nucleon coordinates’’ that take account

of the antisymmetrization effects, and then the Pauli blocking in the final state is automatically introduced.<sup>1),2)</sup>

The third term  $\Delta\mathbf{Z}_i(t)$  is a stochastic term for the wave packet splitting mentioned above.<sup>8),28),29)</sup> The change of the width and shape of each wave packet is calculated by solving the Vlasov equation (for some time period) with the same effective interaction as for the term  $\{\mathbf{Z}_i, \mathcal{H}\}_{\text{PB}}$ . An essential ingredient here is how long the coherent single-particle motion is solved before decoherence. The properties of fluctuations  $\Delta\mathbf{Z}_i(t)$  are determined depending on this time scale called coherence time  $\tau$ . When the wave packet splitting was first introduced into AMD,<sup>8),28)</sup> the limit of  $\tau \rightarrow 0$  was taken, for which the decoherence effect is maximum. The choice of a finite coherence time has been formulated in Ref. 29), and a reasonable choice may be to consider decoherence for a nucleon when it collides with another nucleon. This choice is symbolically denoted by  $\tau = \tau_{\text{NN}}$ , though  $\tau$  is not a constant number.

The last term  $\mu(\mathbf{Z}_i, \mathcal{H}')$  is a dissipation term related to the fluctuation term  $\Delta\mathbf{Z}_i(t)$ . This term is necessary in order to restore the energy conservation that is violated by the fluctuation term. The coefficient  $\mu$  is given by the condition of energy conservation. However, the form of this term is somehow arbitrary. The variables  $Z$  are shifted to the direction of the gradient of the energy expectation value  $\mathcal{H}$  under the constraints of nine conserved quantities (the center-of-mass variables and the total angular momentum). When the number of other nucleons around the nucleon  $i$  within a phase space radius of  $|\mathbf{Z}_j - \mathbf{Z}_i| < 2.5$  is more than a certain number  $N_{c9}$ , other twelve global one-body quantities (monopole and quadrupole moments in coordinate and momentum spaces) are also included as constrained quantities for the dissipation corresponding to the fluctuation  $\Delta\mathbf{Z}_i(t)$ . The latter constraints should be imposed because the one-body time evolution has already been considered by  $\{\mathbf{Z}_i, \mathcal{H}\}_{\text{PB}} + \Delta\mathbf{Z}_i(t)$ . Empirically,  $N_{c9}$  has been chosen between 5 and 15.

A summary of the complete formulation of AMD for reactions can be found in Ref. 4).

### §3. Applications of time-independent AMD method to nuclear structure

We here discuss some topics investigated with the time-independent AMD method focusing on cluster aspects.

#### 3.1. Molecular structures in Be and Ne isotopes

Cluster structure of Be isotopes is one of the fascinating subjects of unstable nuclei. A  $2\alpha$ -cluster core is favored in neutron-rich Be isotopes as well as  ${}^8\text{Be}$  whose ground state is a  $2\alpha$  resonance state. The low-lying states of neutron-rich Be isotopes are described well by a molecular-orbital picture based on a  $2\alpha$  core and valence neutrons moving around the  $2\alpha$ .<sup>30),31),32),33),34),35),36)</sup> In contrast to the molecular-orbital structures in low-lying states, developed di-cluster states such as  ${}^6\text{He}+{}^6\text{He}$  in  ${}^{12}\text{Be}$  have been suggested in highly excited states.<sup>7),35),37),38),39)</sup> There, valence neutrons are moving not around the whole system but around one of two  $\alpha$  clusters. It means that a variety of cluster structures coexist in neutron-rich Be isotopes where

valence neutrons play important roles.

The molecular-orbital picture has been extended also to Ne isotopes such as  $^{21}\text{Ne}$  and  $^{22}\text{Ne}$  based on an  $^{16}\text{O}+\alpha$ -cluster core and valence neutrons in molecular orbitals.<sup>7),32),40)</sup> Di-cluster states like  $^{18}\text{O}+\alpha$ -cluster states in  $^{22}\text{Ne}$  is another attractive subject.<sup>7)</sup>

### 3.1.1. Molecular-orbital structure

The idea of the molecular orbitals surrounding a  $2\alpha$  core was suggested in  $^9\text{Be}$  with a  $2\alpha+n$  cluster model<sup>41)</sup> in 1970's. In 1980's and 1990's, molecular-orbital models were applied to neutron-rich Be isotopes and succeeded to describe rotational bands.<sup>30),31),32),33)</sup>

In a  $2\alpha$  system, molecular orbitals are formed by a linear combination of  $p$  orbits around two  $\alpha$  clusters. In neutron-rich Be isotopes, valence neutrons occupy the molecular orbitals around the  $2\alpha$  core. The negative-parity orbital is called ' $\pi$  orbital', while the longitudinal orbital with positive parity is ' $\sigma$  orbital' (Fig.3). Since the  $\sigma$  orbital has two nodes along the  $\alpha$ - $\alpha$  direction, it gains the kinetic energy as the  $2\alpha$  cluster develops. The energy gain of the  $\sigma$  orbital in the developed  $2\alpha$  system results in the intruder configurations of the  $^{11}\text{Be}$  and  $^{12}\text{Be}$  ground states. In other words, it is the origin of the breaking of the neutron magic number  $N = 8$  in the Be isotopes.

In analogy to neutron-rich Be isotopes, molecular-orbital structures in Ne isotopes have been suggested from the experimental systematics.<sup>32)</sup> Indeed, AMD calculation has predicted the presence of the molecular-orbital bands with  $^{16}\text{O}+\alpha$ -cluster core surrounded by two valence neutrons in the  $\sigma$  orbital.<sup>7),40)</sup> Different from Be isotopes,  $\sigma$  orbital is a linear combination of  $sd$  orbits around  $^{16}\text{O}$  and  $p$  orbits around  $\alpha$  and it results in a  $pf$ -shell like molecular orbital. Another difference is the parity asymmetry of the core, that produces parity doublet of the molecular bands. Similar molecular-orbital structures have been also suggested for F isotopes.<sup>42)</sup> Detailed discussions are given in later sections.

### 3.1.2. Cluster structures in neutron-rich Be isotopes

Cluster structures of Be isotopes have been intensively investigated in many theoretical works with cluster models,<sup>39),43),44),45)</sup> molecular-orbital models,<sup>30),31),33),36),41)</sup> and AMD.<sup>6),34),38),46),47)</sup> In the cluster and molecular-orbital models, the existence of two  $\alpha$  clusters are *a priori* assumed. On the other hand, AMD does not rely on model assumptions of the existence of cluster cores. Nevertheless, the results of AMD calculations indeed indicate the appearance of the  $2\alpha$  core surrounded by valence neutrons in the molecular orbitals in low-lying states of Be isotopes. It means that the formation of the  $2\alpha$  core and molecular orbitals has been theoretically confirmed by those AMD calculations without assuming clusters. Here we discuss the cluster structures of neutron-rich Be isotopes based on AMD calculations.<sup>6),38),46),47)</sup>

The systematic study of the ground and excited states of Be isotopes was performed with VAP calculations in the AMD model (AMD-VAP). Many rotational bands having the  $2\alpha$  core structure were obtained in the theoretical results. In Fig. 5, density distributions of the intrinsic wave functions for the band-head states of  $^{10}\text{Be}$  and  $^{12}\text{Be}$  are shown. As is seen, the proton-density distribution indicates

the formation of the  $2\alpha$  core, while the neutron density distribution exhibits the behavior of valence neutrons around the  $2\alpha$  core.

In analysis of single-particle wave functions in the AMD wave functions, valence neutron orbits in low-lying states of Be isotopes were found to be associated with the molecular orbitals around the  $2\alpha$  core. In Fig. 4, we show schematic figures of the cluster states suggested in  $^{10}\text{Be}$ ,  $^{11}\text{Be}$ , and  $^{12}\text{Be}$ . In the figure, we show the number of neutrons occupying the  $\sigma$ -like orbitals, which have dominant positive-parity components and are regarded as the  $\sigma$  orbital. The experimental value for the excitation energies of the corresponding states are also shown in the figure.

In  $^{10}\text{Be}$ , the valence neutron configurations of  $^{10}\text{Be}(0_1^+)$ ,  $^{10}\text{Be}(1^-)$ , and  $^{10}\text{Be}(0_2^+)$  can be regarded as  $\pi^2$ ,  $\pi\sigma$ , and  $\sigma^2$  configurations meaning two neutrons in the  $\pi$  orbitals, one neutron in the  $\pi$  and the other neutron in the  $\sigma$ , and two neutrons in the  $\sigma$ , respectively. Spatial distributions of the single-particle orbits of valence neutrons in  $^{10}\text{Be}(0_1^+)$  and  $^{10}\text{Be}(0_2^+)$  are shown in Fig. 3(a), where the  $\pi$ -like orbital and the  $\sigma$ -like orbital are clearly seen. Similarly to  $^{10}\text{Be}$ , it was found that the  $^{11}\text{Be}(1/2^+)$ ,  $^{11}\text{Be}(1/2^-)$ , and  $^{11}\text{Be}(3/2_2^-)$  states correspond to  $\pi^2\sigma$ ,  $\pi^3$  and  $\pi\sigma^2$  configurations, while the  $^{12}\text{Be}(0_1^+)$ ,  $^{12}\text{Be}(0_2^+)$ , and  $^{12}\text{Be}(1_1^-)$  states are roughly interpreted as  $\pi^2\sigma^2$ ,  $\pi^4$  and  $\pi^3\sigma^1$  configurations.

Interestingly, the degree of the  $2\alpha$ -cluster development strongly correlates with the number of valence neutrons in the  $\sigma$  orbital. Namely, the  $2\alpha$  cluster develops as the neutron number in the  $\sigma$  orbital increases. It is easily understood because the single-particle energy of the  $\sigma$  orbital decreases because of the kinetic energy gain in largely distant  $2\alpha$  systems. The enhancement of the  $2\alpha$  cluster with neutrons in the  $\sigma$  orbital is consistent with the arguments in Refs. 31), 32), 33). On the other hand, as the neutron number in the  $\pi$  orbitals increases, the cluster structure tends to weaken.

Another interesting characteristic in Be isotopes is the breaking of neutron magicity in  $^{11}\text{Be}$  and  $^{12}\text{Be}$ . The breaking of the  $p$  shell for the neutron magic number  $N = 8$  in  $^{11}\text{Be}$  has been experimentally known from the unnatural parity  $1/2^+$  ground state, while that in  $^{12}\text{Be}$  has been suggested from slow  $\beta$  decay.<sup>48)</sup> Those exotic features of  $^{11}\text{Be}$  and  $^{12}\text{Be}$  can be understood from the molecular orbital picture. The ground states of  $^{11}\text{Be}$  and  $^{12}\text{Be}$  are considered to have dominant intruder configurations with  $\sigma$ -orbital neutron(s) instead of normal  $0\hbar\omega$  configurations. The ground  $1/2^+$  state of  $^{11}\text{Be}$  corresponds to the  $\pi^2\sigma$  configuration, while  $^{12}\text{Be}(0_1^+)$  is the intruder state  $\pi^2\sigma^2$  in terms of molecular orbitals. In the one-center shell-model limit, the  $\pi$  and the  $\sigma$  orbitals correspond to the  $p$  and  $sd$  orbits. Therefore, in the ground states,  $^{11}\text{Be}(1/2_1^+)$  and  $^{12}\text{Be}(0_1^+)$  have dominant  $1\hbar\omega$  and  $2\hbar\omega$  configurations, respectively, indicating the vanishing of the  $N = 8$  magic number in  $^{11}\text{Be}$  and  $^{12}\text{Be}$ . The breaking of the neutron shell in neutron-rich Be isotopes is caused by the lowering  $\sigma$  orbital in the developed  $2\alpha$  structures as discussed in Refs. 6), 38), 47). Again, the  $\sigma$  orbital in the  $2\alpha$  structure plays an important role.

In addition to molecular-orbital structures in such low-lying states, the AMD results for  $^{12}\text{Be}$  suggested molecular resonant states having di-cluster  $^6\text{He}+^6\text{He}$  and  $^8\text{He}+\alpha$  structures in highly excited states.<sup>38)</sup> The result is consistent with the experimental observations of cluster states in He+He break-up reactions<sup>49), 50)</sup> and also

with theoretical suggestions by cluster model calculations.<sup>37),39),51)</sup>

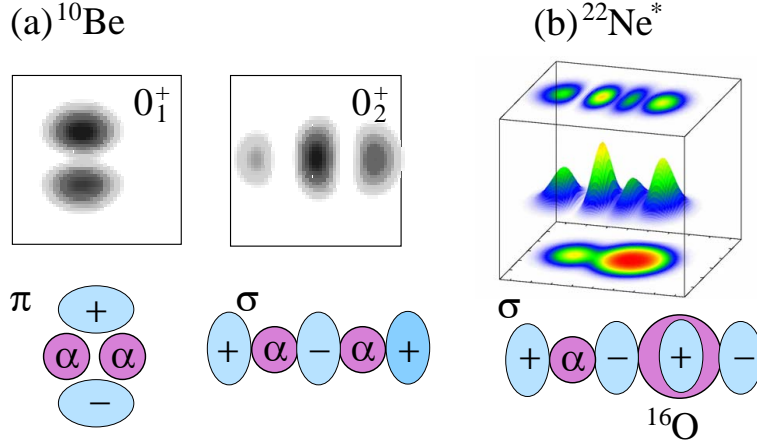


Fig. 3. (a) Density distributions of the single-particle wave functions for valence neutrons in  $^{10}\text{Be}(0_1^+)$  and  $^{10}\text{Be}(0_2^+)$ .<sup>46)</sup> Schematic figure of the molecular orbitals,  $\pi$  and  $\sigma$  orbitals around the  $2\alpha$  core are also shown at the bottom. (b) Density distribution of the excited band ( $K^\pi = 0^-$ ) in  $^{22}\text{Ne}$  obtained by AMD.<sup>40)</sup> The middle and top figures show the density distribution of the single-neutron wave function of the highest single-particle level. The matter density of the total system is displayed at the bottom of the box.

### 3.2. Three-body cluster states in $^{12}\text{C}$ , $^{11}\text{B}$ , and $^{14}\text{C}$ .

One of the typical examples where cluster and shell features coexist is  $^{12}\text{C}$ . The ground state of  $^{12}\text{C}$  is an admixture of  $3\alpha$ -cluster and  $p_{3/2}$ -shell closure structures. On the other hand, a variety of  $3\alpha$ -cluster states have been suggested in excited states in many  $3\alpha$  model calculations since 1970's.<sup>52)</sup> Recently, Tohsaki *et al.* have proposed a new concept of cluster structure in the second  $0^+$  state of  $^{12}\text{C}$ , where three  $\alpha$  clusters are weakly interacting like a gas.<sup>53),54)</sup> Because of the bosonic behavior of  $\alpha$  particles in a dilute  $3\alpha$  gas state this phenomenon has been discussed in relation with Bose-Einstein Condensation of  $\alpha$  particles in a dilute nuclear matter.<sup>55)</sup> It is a challenging issue to search for such dilute cluster gas-like states in other nuclei, for instance,  $^{11}\text{B}$  and  $^{13}\text{C}$ . Another interesting problem to be solved is a linear-chain  $3\alpha$  structure.<sup>56)</sup> It has been a long-standing problem whether a linear-chain  $3\alpha$  state appears in excited states of  $^{12}\text{C}$  or not. Possibility of linear-chain structures in neutron-rich C isotopes is also attracting a great interest as it might be stabilized by valence neutrons.

Applying the AMD method to  $^{12}\text{C}$ ,  $^{11}\text{B}$ , and  $^{14}\text{C}$ , we have found various three-body cluster structures in their excited states as well as shell-model structures in low-lying states. Some are weakly interacting three-cluster states, and some shows rather geometric configurations of clusters. We here discuss cluster aspects of these nuclei based on the AMD-VAP calculations for  $^{12}\text{C}$  and  $^{11}\text{B}$ <sup>10),57),58)</sup> and the  $\beta$ - $\gamma$  constraint AMD calculations for  $^{14}\text{C}$ .<sup>59)</sup>

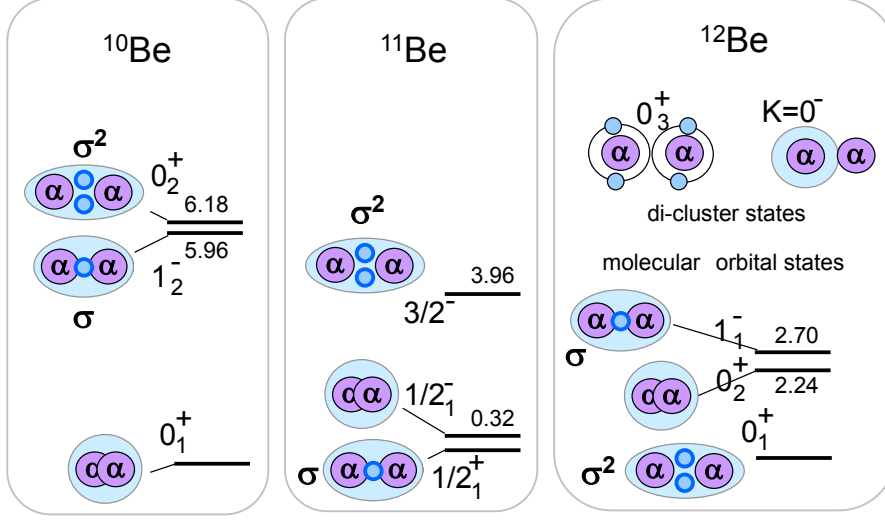


Fig. 4. Schematic figures for cluster states suggested in  $^{10}\text{Be}$ ,  $^{11}\text{Be}$ , and  $^{12}\text{Be}$ . For the molecular-orbital states, 2  $\alpha$  cores and the valence neutrons in the  $\sigma$  orbital are illustrated. The experimental values of the excitation energies are also shown.

### 3.2.1. Cluster structures of $^{12}\text{C}$

To investigate excited states of  $^{12}\text{C}$  we performed the AMD-VAP calculations. As already mentioned, in the AMD model, all nucleons are independently treated without assuming existence of any clusters. The formation or breaking of shell structure and clusters is expressed in the twelve-nucleon dynamics after the energy variation. Even though any clusters are not *a priori* assumed,  $\alpha$  clusters are formed in many excited states of  $^{12}\text{C}$ . Indeed, a variety of  $3\alpha$  cluster states were obtained in the AMD results. The experimental and calculated energy levels of  $^{12}\text{C}$  are shown in Fig. 6, and density distribution of intrinsic wave functions for the ground and excited states is shown in the upper row of Fig. 7. It should be stressed that this is the first calculation that succeeded in simultaneously reproducing the energy spectra of the ground band and those of excited states having developed  $3\alpha$  cluster structures in  $^{12}\text{C}$ . The success owes to flexibility of AMD wave functions which can describe both shell-model and cluster structures. The calculation also reproduces well transition properties such as  $E2$ , monopole, and GT transitions. In the result, the ground state shows the  $p_{3/2}$ -shell closure configuration with a mixing of the  $3\alpha$ -core component, while the second  $0^+$  state has a well-developed  $3\alpha$  cluster structure. Since the  $0_2^+$  wave function has large overlap with various  $3\alpha$  configurations (amplitudes of the superposed wave functions do not concentrate on a specific AMD wave function but they fragment largely into various AMD wave functions), this state is regarded as the  $3\alpha$  gas-like state, where three  $\alpha$  clusters are rather freely moving in a dilute density. The  $3\alpha$  chain-like state was suggested in the third  $0^+$  state around 10 MeV

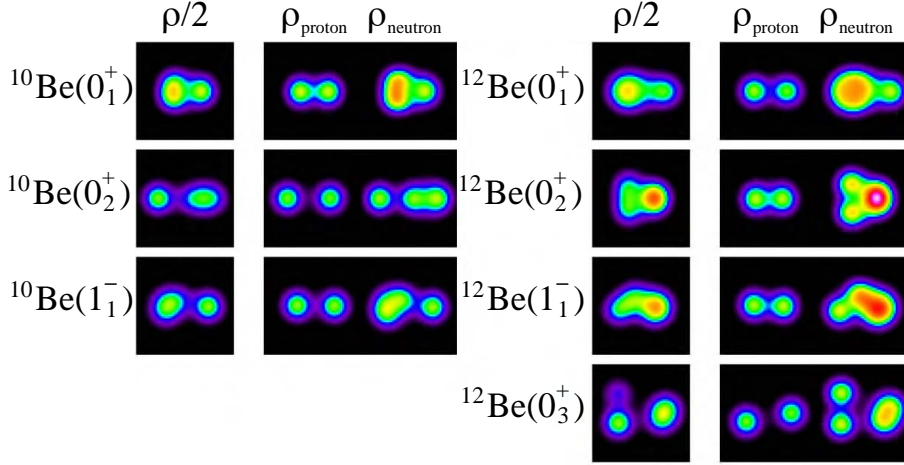


Fig. 5. Density distributions of the intrinsic states for the band-head states of  $^{10}\text{Be}$  and  $^{12}\text{Be}$  obtained by AMD-VAP.<sup>46),38)</sup> The integrated densities of matter, proton and neutron densities are presented in the left, middle and right panels.

in the AMD result. It is not a "linear" chain but it shows an obtuse triangle  $3\alpha$  configuration as seen in the figure. These results are quite similar to those calculated with FMD with the unitary correlation operator method (UCOM).<sup>60)</sup>

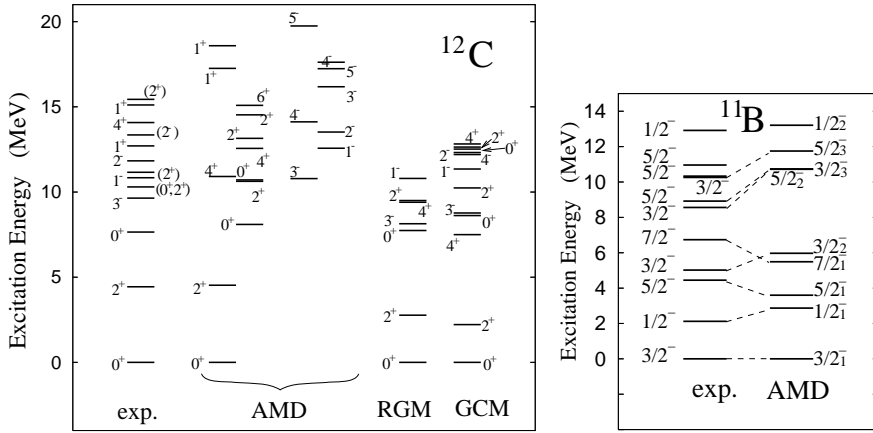


Fig. 6. Left: Energy levels of  $^{12}\text{C}$  calculated with AMD-VAP.<sup>57)</sup> The theoretical levels of  $^{12}\text{C}$  calculated with the  $3\alpha\text{RGM}$ <sup>61)</sup> and  $3\alpha\text{GCM}$ <sup>62)</sup> are also shown. Right: Energy levels of  $^{11}\text{B}$  calculated with AMD-VAP.<sup>58)</sup>

### 3.2.2. Cluster structures of $^{11}\text{B}$

We applied the same method, AMD-VAP, to  $^{11}\text{B}$  and its mirror nucleus  $^{11}\text{C}$ , and investigated the structures while focusing on cluster aspect. The energy levels of negative-parity states of  $^{11}\text{B}$  were reasonably reproduced by the calculations as



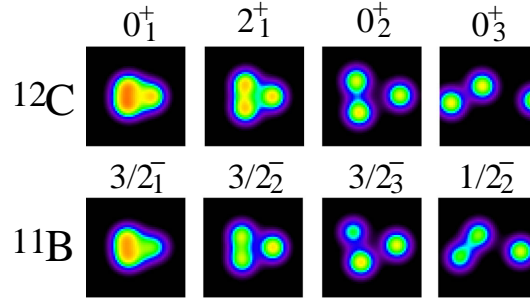


Fig. 7. Density distributions of intrinsic states for the ground and excited states of  $^{12}\text{C}$  and  $^{11}\text{B}$  calculated by AMD-VAP.<sup>57),58)</sup>

shown in Fig. 6.

The  $3/2_3^-$  states at the excitation energy  $E^* \sim 8$  MeV,  $^{11}\text{B}(3/2_3^-, 8.65$  MeV) and  $^{11}\text{C}(3/2_3^-, 8.10$  MeV) are experimentally known to have abnormal properties such as weak GT and  $M1$  transitions compared with normal low-lying states. It is also interesting that the  $3/2_3^-$  state is missing in shell-model calculations for  $^{11}\text{B}$ . These facts suggest that the  $3/2_3^-$  may not be ordinary shell-model-like state but may have a developed cluster structure. The AMD calculations for  $^{11}\text{B}$  give good results for the energy levels including the  $3/2_3^-$  state (Fig. 6) and reproduce well the experimental values of transition strengths. For the  $3/2_3^-$  state, the quenched GT and  $M1$  transitions are understood because of the developed cluster structure of the  $3/2_3^-$  state which has small overlap with the low-lying shell-model-like states. Indeed, the  $3/2_3^-$  states of  $^{11}\text{C}$  and  $^{11}\text{B}$  exhibit the remarkably developed  $2\alpha+^3\text{He}$  and  $2\alpha+t$  clustering (Fig. 7).

### 3.2.3. Analogy of cluster aspects of $^{11}\text{B}$ to $^{12}\text{C}$

Comparing the results for  $^{11}\text{B}$  with those for  $^{12}\text{C}$ , we found good analogies of cluster aspects between  $^{11}\text{B}$  and  $^{12}\text{C}$ . As shown in Fig. 7, the ground state of  $^{11}\text{B}$  is described by the  $p_{3/2}$ -shell configuration with a mixing of cluster structure as well as that of  $^{12}\text{C}$ . The development of the  $2\alpha+t$ -cluster core in the  $^{11}\text{B}(3/2_2^-)$  shows a good analogy to that of the  $3\alpha$ -cluster core in the  $^{12}\text{C}(2_1^+)$ . The remarkably developed  $2\alpha+t$ -cluster structures in the  $^{11}\text{B}(3/2_3^-)$  and  $^{11}\text{B}(1/2_2^-)$  can be associated with the developed  $3\alpha$  cluster in the  $^{12}\text{C}(0_2^+)$  and  $^{12}\text{C}(0_3^+)$ , respectively.

Particular attention is paid to analogy of  $^{11}\text{B}(3/2_3^-)$  to  $^{12}\text{C}(0_2^+)$ . Similarly to the case of  $^{12}\text{C}(0_2^+)$ , the  $^{11}\text{B}(3/2_3^-)$  wave function has large overlap with various  $2\alpha+t$  configurations indicating that the state has no geometric cluster configuration but it should be regarded as a weakly interacting  $2\alpha+t$ -cluster state. The root-mean-square radius (r.m.s.r.) of the  $^{11}\text{B}(3/2_3^-)$  state is 3.1 fm and it is remarkably large compared with that of the ground state (2.5 fm). Considering amplitudes of the wave function fragmented on various configurations and the large radius, the  $3/2_3^-$  state may be a  $2\alpha+t$ -cluster state with a dilute density like a gas, where clusters are rather freely moving. It should be noted that, for the  $^{11}\text{B}(3/2_3^-)$ , the energy position relative to the three-cluster break-up threshold is lower and the nuclear size

is smaller than those for  $^{12}\text{C}(0_2^+)$ , and therefore the gas-like feature of the  $^{11}\text{B}(3/2_3^-)$  might be weaker than the  $^{12}\text{C}(0_2^+)$ .

Another analogy between  $^{11}\text{B}(3/2_3^-)$  and  $^{12}\text{C}(0_2^+)$  is remarkable monopole transition strengths from the ground state. The calculated iso-scalar monopole strength  $B(IS0)$  for the transition  $3/2_1^- \rightarrow 3/2_3^-$  is  $94 \text{ fm}^4$  and the value is in good agreement with the experimental value  $94 \pm 16 \text{ fm}^4$ .<sup>63)</sup> The  $B(IS0)$  value is as large as that for the monopole transition  $0_1^+ \rightarrow 0_2^+$  in  $^{12}\text{C}$ .

Recently, structures of  $^{11}\text{B}$  has been investigated also by  $2\alpha+t$  orthogonality condition model (OCM).<sup>64)</sup> In the results of  $2\alpha+t$  OCM, different cluster features between  $^{11}\text{B}(3/2_3^-)$  and  $^{12}\text{C}(0_2^+)$  have been pointed out from the point of view of  $\alpha$  condensation. Cluster gas features of  $^{11}\text{B}$  are under discussion.

### 3.2.4. Cluster structures of $^{14}\text{C}$

As mentioned, the straight-line chain structure of three  $\alpha$  clusters may not be stable in  $^{12}\text{C}$  even though the linear-chain-like  $3\alpha$  state with the obtuse triangle configuration might exist in the  $0_3^+$  state. We here consider cluster structures of  $^{14}\text{C}$ , in which  $3\alpha$ -core structures with additional two neutrons are expected.

Structures of excited states of  $^{14}\text{C}$  were investigated with a method of  $\beta$ - $\gamma$  constraint AMD in combination with GCM by Suhara and one of the authors (Y. K-E.).<sup>59)</sup> We stress again that existence of clusters was not assumed in the model but dynamics of fourteen nucleons was solved in the AMD model space. The results suggested a variety of developed  $3\alpha$ -cluster core structures in excited states. One of the new findings is that a  $3\alpha$  linear-chain structure with valence neutrons can be stabilized in  $^{14}\text{C}$  and may construct a  $K^\pi = 0^+$  rotational band above the  $^{10}\text{Be}+\alpha$  threshold energy (Fig. 8). As shown in the density distributions of protons and neutrons, the linear-chain state indicates a strongly coupling  $^{10}\text{Be}+\alpha$  cluster structure, where an  $\alpha$  cluster is sitting on the head of a deformed  $^{10}\text{Be}$  cluster. It was found that additional neutrons play an important role to stabilize the linear-chain configuration. Unfortunately, there is no experimental evidence for the linear-chain state. The  $^{10}\text{Be}+\alpha$  decay observations<sup>65),66)</sup> would be helpful to identify it.

### 3.3. Spectroscopy and exotic phenomena in the island of inversion

Neutron-rich Ne and Mg isotopes around the  $N \sim 20$  region called ‘‘island of inversion’’ are known to have anomalous properties.<sup>68)</sup> These anomalies originate in the quenching of the  $N = 20$  shell gap in the neutron-rich nuclei and it leads to the breakdown of the magic number  $N = 20$  and large nuclear deformation. This drastic change of nuclear shell structure has been intensively investigated mainly focusing on the spectral properties of yrast states.<sup>69),70),71),72),73),74)</sup> Recently thanks to the development of the experimental technique, the information of the non-yrast states<sup>75),76),77),78)</sup> is rapidly increasing to reveal exotic phenomena peculiar to the island of inversion. For example, ‘‘the coexistence of spherical and deformed shapes’’ and ‘‘the coexistence of normal and intruder configurations’’ have been discussed based on the finding of the second excited  $0^+$  states of  $^{30}\text{Mg}$ <sup>76)</sup> and  $^{32}\text{Mg}$ .<sup>78)</sup>

AMD combined with GCM is one of the powerful theoretical approaches to investigate the non-yrast states of nuclei in the island of inversion as well as the

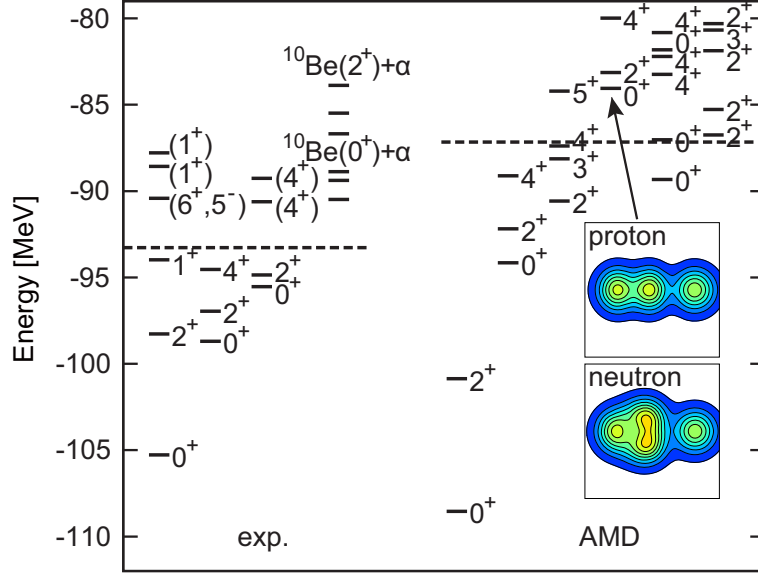


Fig. 8. Energy levels of  $^{14}\text{C}$ . The theoretical data are those in Ref. 59) calculated with  $\beta - \gamma$  constraint AMD with GCM by using the Volkov No.2 force with  $B = H = 0.125$ ,  $M = 0.60$  and the G3RS-type spin-orbit force with  $u_I = -u_{II} = 1600$  MeV. Proton and neutron density distributions for the linear-chain  $K^\pi = 0^+$  band are also shown. The dotted lines are the experimental and theoretical  $^{10}\text{Be} + \alpha$  threshold energies. The figure is taken from Ref. 67).

yrast states.<sup>6),7),79),80),81),82)</sup> We here introduce some recent AMD studies for shape coexistence, one-neutron halo and molecular structure in the island of inversion.

### 3.3.1. Many-particle and many-hole states and shape coexistence in $^{31}\text{Mg}$

The neutron orbits and the coexistence of normal and intruder configurations in neutron-rich Ne and Mg isotopes are most sensitively probed by the low-lying yrast and non-yrast states of odd-mass isotopes. The last neutron's orbit, which determines the spin and parity of the ground state, is quite sensitive to the nuclear deformation.

As one of such examples, Fig. 9 shows the calculated energy surface, and predicted<sup>81)</sup> and observed spectrum of  $^{31}\text{Mg}$ .<sup>84),85),86),87),88),90),89),83)</sup> The energy surface of  $^{31}\text{Mg}$  (Fig. 9 (a)) has the low-lying local minima with different nuclear deformations. By calculating the occupation probabilities of single-particle orbits, these local minima are found to correspond to the  $0p1h$ ,  $1p2h$ ,  $2p3h$  and  $3p4h$  neutron configurations in ascending order of deformation. Here the particle-hole configurations are labeled relative to the  $N = 20$  shell closure and nuclear deformation becomes larger as numbers of particles in  $pf$  shell and holes in  $sd$  shell increase. To predict the ground state configuration, it is essential to perform a GCM calculation. In fact, AMD+GCM calculation (Fig. 9 (b)) shows that the ground state is strongly deformed and an almost pure  $2p3h$  configuration in which two neutrons are promoted into  $pf$  shell across the  $N = 20$  shell gap to break down the magic number. The calculated magnetic moment of the ground state is  $-0.91\mu_N$ , while the

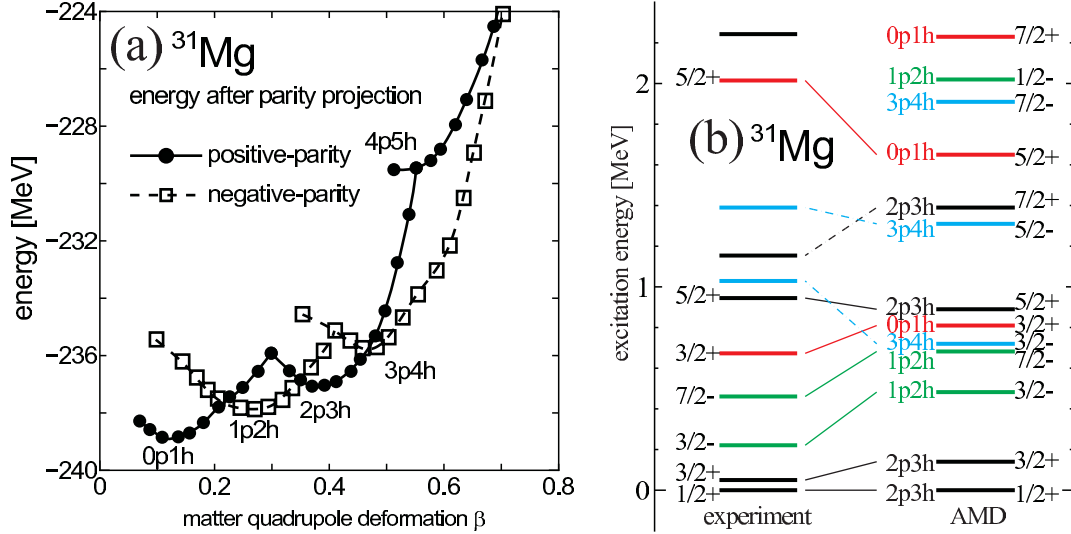


Fig. 9. (a) Energy surfaces of the positive- and negative-parity states of  $^{31}\text{Mg}$  as function of quadrupole deformation parameter  $\beta$  calculated by AMD. The AMD results are taken from Ref. 81). (b) Low-lying spectrum of  $^{31}\text{Mg}$  calculated by AMD+GCM compared with the experimental assignment suggested in Ref. 83).

observed value is  $-0.88\mu_N$ .<sup>84)</sup> Since the spherical  $0p1h$  states in which the  $N = 20$  magicity is retained give positive magnetic moment, the breakdown of the  $N = 20$  magic number is confirmed without ambiguity. AMD predicts that the ground state is followed by  $3/2_1^+$ ,  $5/2_1^+$  and  $7/2_1^+$  states with  $2p3h$  configuration to constitute the rotational ground band due to the strong deformation. Furthermore, due to the quenching of the  $N = 20$  shell gap, coexistence of three different configurations at small excitation energy is also predicted. The  $1p2h$  configuration appears as the  $3/2_1^-$  and  $7/2_1^-$  states at very small excitation energies, the strongly deformed  $3p4h$  configuration constitutes the  $K^\pi = 3/2^-$  rotational band starting from 720 keV, and the normal  $0p1h$  configuration appears as the  $5/2_2^+$  state at 1.6 MeV. Most of these excited states have been observed, in good agreement with AMD predictions, by the measurements of  $\beta$ -decays,<sup>85),86),87)</sup> one proton or neutron knockout reactions<sup>89),90)</sup> and Coulomb excitation.<sup>88)</sup> Thus, the coexistence of various neutron configurations and deformed states is now established. For the recent discussions on other nuclei, readers are directed to Ref. 82).

### 3.3.2. Neutron-halo with a deformed core in the island of inversion

As one of the fascinating phenomena in the island of inversion, we focus on the one-neutron halo structure of  $^{31}\text{Ne}$ . Recent experiments at RI Beam Factory in RIKEN have revealed the large Coulomb breakup cross section<sup>91)</sup> and interaction cross section<sup>92),93)</sup> of  $^{31}\text{Ne}$ , and the  $p$ - or  $s$ -wave neutron-halo structure has been suggested from the analysis of the Coulomb breakup.<sup>91),94)</sup> Usually neutron-halo structure has been discussed based on the “spherical inert core + weakly bound neutron” models as done for  $^6\text{He}$  and  $^{11}\text{Li}$ . However, in this case the core nucleus  $^{30}\text{Ne}$  is located in the middle of the island of inversion and the assumption of the

spherical inert core is inadequate. The last neutron of  $^{31}\text{Ne}$  may be coupled to the strongly deformed core with broken magic number. Therefore, the analysis based on a full microscopic theory is more suitable and necessary. Since a single-particle wave

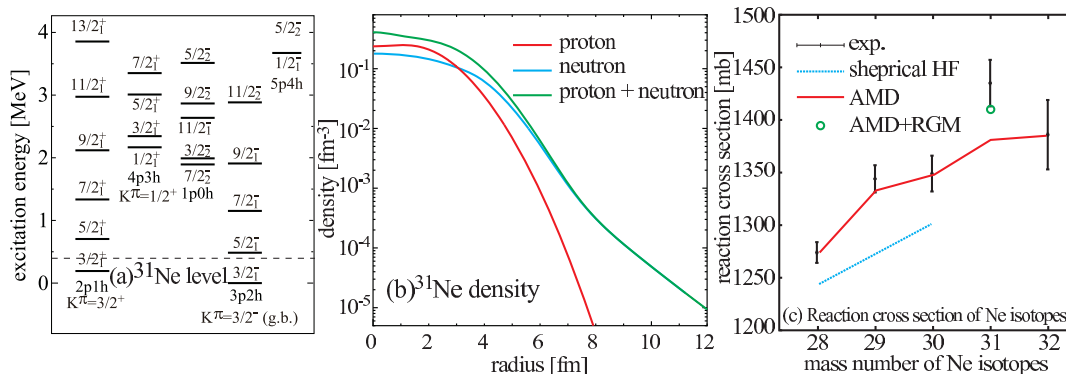


Fig. 10. (a) Low-lying spectrum of  $^{31}\text{Ne}$  calculated by AMD+RGM. Dashed line shows one neutron threshold energy. (b) Proton, neutron, and proton + neutron densities of  $^{31}\text{Ne}$  ground state ( $J^\pi = 3/2^-$ ) calculated by AMD+RGM. (c) Reaction cross section of Ne isotopes calculated by double-folding model using the density distribution obtained by AMD (solid line), AMD+RGM (open circle for  $^{31}\text{Ne}$ ) compared with the observed data.<sup>92),93)</sup> The results are taken from Refs. 82),96).

function is represented by a Gaussian wave packet, AMD cannot describe properly the tail part of halo nucleus which shows the exponential damping. This shortage is overcome by combining AMD with resonating group method (AMD+RGM). We use the RGM-type wave function for  $^{31}\text{Ne}$ ,

$$\Psi_{JM} = \sum_{\alpha l} c_{\alpha l} \mathcal{A} [\chi_{\alpha l}(r) Y_{lm}(\hat{r}) \phi_n \phi_{30\text{Ne}}(\alpha)]_{JM}, \quad (3.1)$$

where  $\phi_n$  and  $\chi_{\alpha l}(r) Y_{lm}(\hat{r})$  are the spin wave function of the valence neutron and the relative motion between the valence neutron and  $^{30}\text{Ne}$ , respectively.  $\phi_{30\text{Ne}}(\alpha)$  is the internal wave function of  $^{30}\text{Ne}$  solved by AMD+GCM,<sup>80)</sup> and  $\alpha$  labels the ground and excited states of  $^{30}\text{Ne}$ . Since the AMD wave function of  $^{30}\text{Ne}$  is a superposition of Slater determinant of Gaussians, the coefficients  $c_{\alpha l}$  and the relative wave function  $\chi_{\alpha l}(r)$  can be solved by transforming Eq. (3.1) into a GCM type wave function. Recent development of high-performance computing enabled this CPU demanding calculation.

Figure 10 (a) shows the predicted spectrum of  $^{31}\text{Ne}$  by AMD+RGM. The ground state is the  $3/2^-$  state and the calculated one neutron separation energy is  $S_n = 0.45$  MeV, while the observed value is  $0.29 \pm 1.64$  MeV.<sup>95)</sup> Due to this small separation energy, the density distribution of  $^{31}\text{Ne}$  calculated by AMD+RGM shows the long tail at large distance indicating a  $p$ -wave halo ( $1p_{3/2}$ -neutron coupled to  $^{30}\text{Ne}$ ) as shown in Fig. 10 (b). The effect of the deformed core appears as the core excitation. From the coefficients  $c_{\alpha l}$ , it is found that the  $p_{3/2} \otimes ^{30}\text{Ne}(2^+)$  configuration amounts to 41%, that is larger than the  $p_{3/2} \otimes ^{30}\text{Ne}(0^+)$  configuration which amounts to 37%. These values suggest that the  $p_{3/2}$  neutron is coupled to the deformed and

rotating ground band of  $^{30}\text{Ne}$ . Using AMD and AMD+RGM wave functions, the reaction cross sections of  $^{31}\text{Ne}$  and other Ne isotopes are analyzed based on the double-folding model.<sup>96),97)</sup> Figure 10 (c) compares the calculated and observed reaction cross section. We can see that AMD wave function shows overall agreement with the observation except for  $^{31}\text{Ne}$ , and anomalous large cross section of  $^{31}\text{Ne}$  is reasonably described by employing the AMD+RGM wave function. Thus, with a help of high-performance computing, AMD combined with RGM and reaction theory is a promising method to investigate neutron-halo nuclei and their reactions in heavier mass region. We can find many other candidates of weakly bound system such as  $^{35}\text{Mg}$  and  $^{37}\text{Mg}$  from the systematics of the binding energy, and analysis of them is now ongoing.

### 3.3.3. Molecule-like states in the island of inversion

Another example of exotic phenomena in the island of inversion is the molecule-like structure at highly excited region. As discussed in the subsection 3.1, several excited states of O, F and Ne isotopes have been predicted to have molecule-like structure analogous to Be isotopes.<sup>40),98)</sup> Especially, the candidates of molecule-like states have been recently observed in  $^{18\sim 20}\text{O}$ <sup>99),100),101)</sup> and found to qualitatively agree with the AMD predictions.<sup>98)</sup> Thus the exploration of molecule-like structure is expanding to heavier neutron-rich systems. In the case of F and Ne isotopes, since the neutron drip line is farther extended than for O isotopes, we can expect molecule-like structure with more valence neutrons and more exotic phenomena.

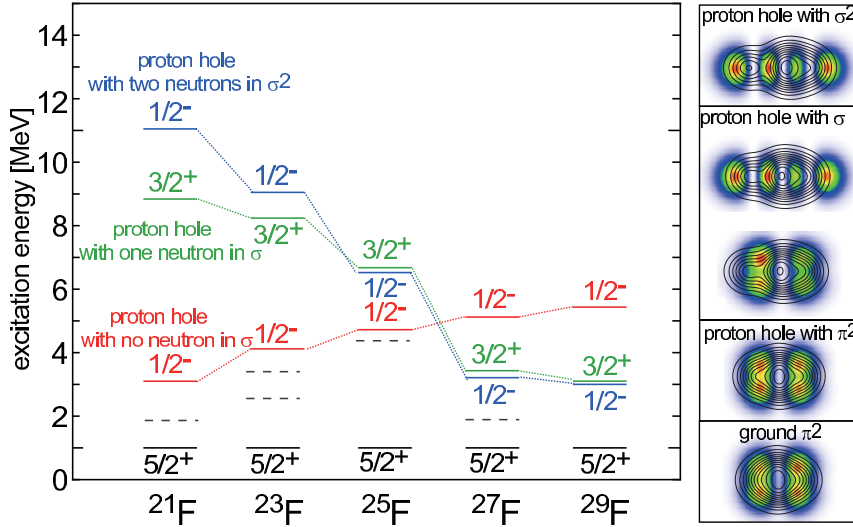


Fig. 11. Left: Band-head energies of proton hole states of F isotopes. Red lines show the states with a proton excitation from  $p$  to  $sd$  shell and no neutron in  $pf$  shell, while green (blue) lines show those with one (two) neutron(s) in  $pf$  shell that have molecule-like structure. Right: Density distribution of the core ( $^{19}\text{F}$ , contour lines) and two valence neutrons (color plot) of  $^{21}\text{F}$ . From top to bottom, each panel corresponds to the states with two, one and no neutrons in  $pf$  shell with a proton hole and the ground state, respectively. This figure is taken from Ref. 7).

Figure 11 shows the energies of the F isotopes obtained by AMD+GCM<sup>42)</sup> as

an example. All of these F isotopes have molecule-like states in their excited states and there are always two kinds of molecular bands (green and blue lines in Fig. 11 left). In these states, one or two valence neutrons are excited into  $\sigma$  orbital ( $pf$  shell) together with a proton excitation from  $p$  to  $sd$  shell, and the  $\alpha+N$  cluster structure develops (Fig. 11 right). It is notable that the drastic reduction of their excitation energies toward the neutron drip line is predicted. To understand this reduction, readers are reminded following points. (1) As mentioned in section 3.1, the  $\sigma$  orbital originates in the  $pf$  shell, and its energy is lowered in the island of inversion due to the quenching of the  $N = 20$  shell gap. (2) If the core has cluster structure, it induces the deformation of the system and it further lowers the energy of  $\sigma$  orbital as in the case of Be isotopes. Therefore, the neutron excitation into  $\sigma$  orbital and  $\alpha$  clustering of the core work in a cooperative way to reduce the excitation energies of molecular states in the island of inversion. Up to now, several candidates for the molecular states in lighter F isotopes are experimentally known.<sup>102),103),104)</sup> More data for F isotopes near the drip line will be experimentally available in near future.

### 3.4. Superdeformation in $sd$ -shell nuclei

A recent development in high-spin physics is the discovery of the superdeformed band at very small mass region ( $A \sim 40$ ) such as  $^{36}\text{Ar}$ ,<sup>105)</sup>  $^{40}\text{Ca}$ <sup>106)</sup> and  $^{44}\text{Ti}$ .<sup>107)</sup> In contrast with heavier nuclei, these superdeformed bands are assigned from high-spin states down to very low-spin states ( $J^\pi = 0^+ \sim 4^+$ ). From this discovery, the low-lying  $0^+$  states known for a long time are now identified as the band-head of the superdeformed bands. On the other hand,  $\alpha$  clustering of low-lying states and molecular structure of highly excited states have long been discussed. AMD studies have been made to investigate properties of superdeformed states and to reveal the relationship between the superdeformed states and cluster states.

#### 3.4.1. Dual nature of superdeformed states and its evolution to the molecular states

The strongly deformed excited state of  $^{32}\text{S}$  is of particular interest because of the following reasons. 1)  $^{32}\text{S}$  ( $N = Z = 16$ ) is a double magic nucleus of superdeformation. A couple of mean-field calculations<sup>108),109),110)</sup> have predicted the superdeformed state around  $E^* \sim 10$  MeV and it has  $4\hbar\omega$  excited configuration relative to the ground state. 2) Using unique optical potential for  $^{16}\text{O}$ - $^{16}\text{O}$  scattering,<sup>111),112)</sup>  $^{16}\text{O}+^{16}\text{O}$  cluster model<sup>113)</sup> showed the presence of three molecular bands. Among them the lowest energy band is located a few MeV below the  $^{16}\text{O}+^{16}\text{O}$  threshold energy and coincides with the predicted superdeformed band mentioned above, while the highest energy band nicely reproduces the well-known  $^{16}\text{O}+^{16}\text{O}$  molecular resonances.<sup>114),115)</sup> Thus the two different theoretical approaches give qualitatively the same result and suggest the relationship between the superdeformed states and cluster states.

AMD gives a unified understanding for the results of the mean-field and cluster model studies and shows that the superdeformed band evolves to the  $^{16}\text{O}+^{16}\text{O}$  molecular bands as the excitation energy increases.<sup>116)</sup> Similar to the mean-field calculations, AMD predicts a well pronounced superdeformed minimum (Fig. 12 (a)). The density distribution of the superdeformed wave function clearly shows  $^{16}\text{O}+^{16}\text{O}$

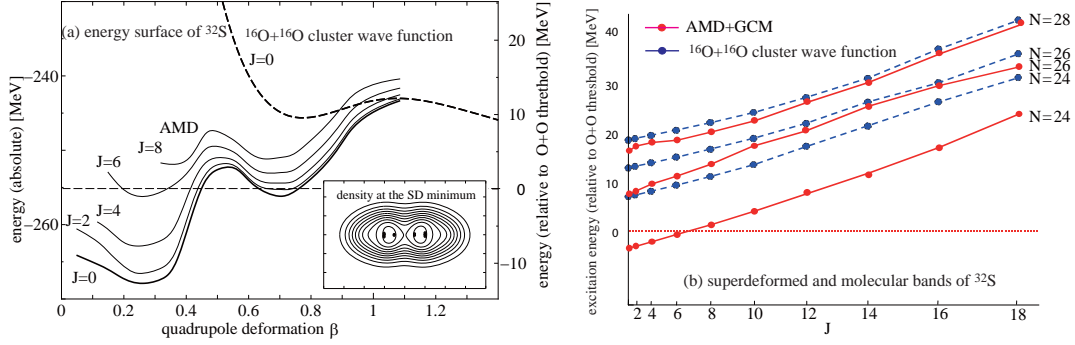


Fig. 12. (a) Energy surface of  $^{32}\text{S}$  as function of quadrupole deformation  $\beta$ . Solid lines show the energy surfaces for each angular momentum obtained by AMD, while the dashed line shows that obtained by  $^{16}\text{O}+^{16}\text{O}$  cluster wave function. (b) Three rotational bands built around the superdeformed minimum obtained by the AMD+GCM (solid lines) and  $^{16}\text{O}+^{16}\text{O}$  cluster model wave functions. The principal quantum number  $N$  for each rotational band is also shown. The figures are taken from Ref. 116).

molecule-like structure and the distance between  $^{16}\text{O}+^{16}\text{O}$  increases as deformation becomes larger. Note that the superdeformed wave function is smoothly connected to the  $^{16}\text{O}+^{16}\text{O}$  cluster wave function around the Coulomb barrier ( $\beta \sim 1.1$ ) in AMD. Around the superdeformed minimum, the  $^{16}\text{O}$  clusters are distorted by the formation of the mean-field and by the spin-orbit interaction to gain more binding energy, while the pure  $^{16}\text{O}+^{16}\text{O}$  cluster structure is restored as inter-cluster distance (deformation) becomes larger. The AMD+GCM calculation has shown that three rotational bands appear as the superposition of the wave functions around this superdeformed minimum (Fig. 12 (b)). The lowest energy band coincides with the superdeformed band predicted by the mean-field calculations. The  $^{16}\text{O}+^{16}\text{O}$  cluster component in this band amounts to 57% which means the superdeformed band has the  $^{16}\text{O}+^{16}\text{O}$  molecule-like structure, but  $^{16}\text{O}$  clusters are considerably distorted. This shows dual nature of this band (mixing of mean-field and cluster nature) and explains why the mean-field calculations and cluster model give qualitatively the same results. The degree-of-freedom of inter-cluster motion embedded in the superdeformed band shows up as two excited rotational bands. The cluster components of these two bands amount to more than 90% and these bands are interpreted as the excitation mode of the superdeformed band in which the relative motion between two  $^{16}\text{O}$  clusters is excited by 2 and 4  $\hbar\omega$ , that are confirmed by the analysis of the inter-cluster motion of the AMD wave function. The highest band with 4 $\hbar\omega$  excitation of relative motion plausibly agrees with the observed  $^{16}\text{O}+^{16}\text{O}$  molecular band.<sup>114),115)</sup> Thus the superdeformed band and the molecular band can be regarded as a series of the  $^{16}\text{O}+^{16}\text{O}$  cluster bands, and the superdeformed band evolves to the  $^{16}\text{O}+^{16}\text{O}$  molecular band as the inter-cluster motion is excited.

### 3.4.2. Superdeformation and clusters in $A \sim 40$ region

The superdeformed state and  $^{16}\text{O}+^{16}\text{O}$  clustering of  $^{32}\text{S}$  shed light on the relationship between the (super)deformed states and clustering. As an illustrative and



interesting example, Fig. 13 (a) shows the observed spectra of doubly magic nucleus  $^{40}\text{Ca}$ . Two deformed rotational bands start from the  $0^+$  states at 3.35 and 5.21 MeV. It has been suggested that the former band is predominated by a  $4\hbar\omega$  excited configuration and the latter is a  $8\hbar\omega$  configuration.<sup>117),118)</sup> The discovery of the high-spin states<sup>106)</sup> identified the latter band as a superdeformed band, and several theoretical studies based on the mean-field models have been performed.<sup>109),110)</sup> On the other hand, based on the cluster model,  $\alpha+^{36}\text{Ar}$  clustering of the band starting from 3.35 MeV has been suggested<sup>119),120)</sup> and experimentally confirmed by the  $\alpha$  transfer reaction on  $^{36}\text{Ar}$ .<sup>121),122)</sup> In the following, we denote the band starting at 3.35 MeV as ND band and the band at 5.21 MeV as SD band.

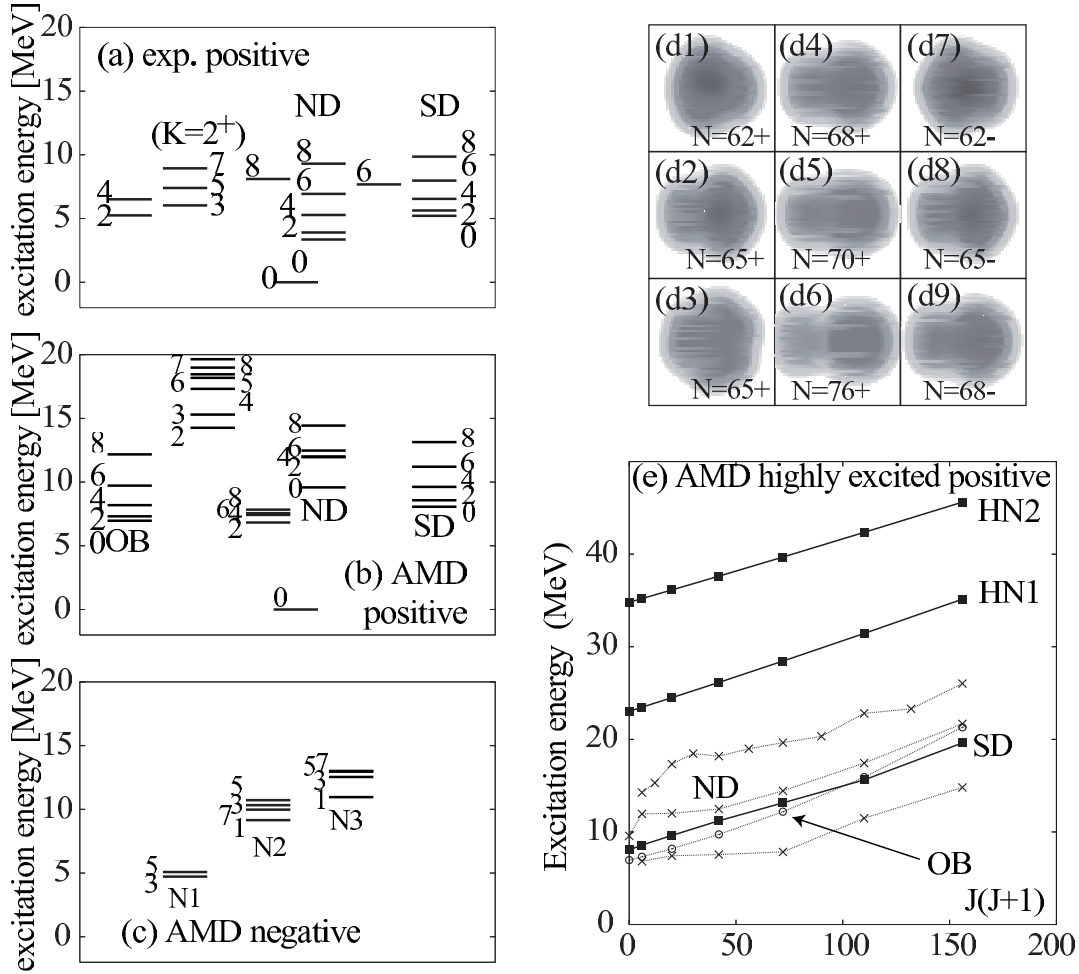


Fig. 13. (a) Observed positive-parity states of  $^{40}\text{Ca}$ . (b) and (c) Calculated positive- and negative-parity spectra by AMD+GCM.<sup>123)</sup> 'OB', 'ND', 'SD' and 'N3' denote the oblate and prolate deformed bands, superdeformed band and parity doublet partner of the superdeformed band, respectively. (d1)-(d9) Intrinsic density distribution obtained by the constraint variational calculation (see text). (e) Calculated spectra of the highly excited positive-parity states. HN1 and HN2 denote the higher nodal  $^{12}\text{C}+^{28}\text{Si}$  cluster bands in which the inter-cluster motion is excited. The AMD results are taken from Ref. 123).

AMD studies have been performed to clarify nature of the ND and SD bands<sup>123), 124)</sup> to reveal the coexistence of the different deformed bands and their relationship to the cluster structure. Here we mainly discuss the result reported in Ref. 123), in which the variational calculation is performed under the constraint on the principal quantum number of the harmonic oscillator,

$$N = \sum_{i=1}^A \hat{a}_i^\dagger \hat{a}_i = \sum_{i=1}^A \left[ \frac{\mathbf{P}_i^2}{4\hbar^2\nu} + \nu \mathbf{r}_i^2 - \frac{3}{2} \right]. \quad (3.2)$$

Here the lowest Pauli allowed value is  $N = 60$ , and the average number of nucleons promoted from  $sd$  to  $pf$  shell increases for a larger value of  $N$ . Figure 13 (d1)-(d9) shows the intrinsic density distributions obtained for different values of  $N$ . For a small value of  $N$ , an almost spherical state is obtained (d1), and prolate (d2) and oblate (d3) deformed states appear by slight increase of  $N$ . Further increase of  $N$  develops the parity asymmetric prolate deformed state (d4). The parity asymmetry of this wave function originates in  $^{12}\text{C}+^{28}\text{Si}$  cluster nature of the superdeformed state, since it evolves into a prominent  $^{12}\text{C}+^{28}\text{Si}$  cluster state as  $N$  increases (d4)-(d6). An important point is that similar  $^{12}\text{C}+^{28}\text{Si}$  cluster-like state (d9) also appears in the negative-parity state with large  $N$ , while the negative-parity state with small  $N$  (d7) corresponds to the  $1\hbar\omega$  excited state built on the spherical state (d1).

Several rotational bands are obtained as the superposition of those wave functions by AMD+GCM as shown in Fig. 13 (b) and (c) compared with the observed data (Fig. 13 (a)). In the positive-parity states, there are two rotational bands (denoted as ND and OB in Fig. 13 (b)) that are dominantly composed of the wave functions (d2) and (d3) respectively, predicting a prolate and oblate shape coexistence. Though the calculated excitation energy is larger than the observation, the calculated ND band is assigned to the observed band starting from 3.35 MeV from the comparison of their  $B(E2)$  strengths, while the corresponding oblate deformed band has not been experimentally assigned yet.

The highlight of the result is the superdeformed band and related ones that are associated with the parity-asymmetric  $^{12}\text{C}+^{28}\text{Si}$  clustering nature (Fig. 13 (d4)-(d6) and (d8)-(d9)). The calculated superdeformed band (SD in Fig. 13 (b)) is dominated by the wave functions (d4)-(d6) and starts around 8 MeV, while the observed band is located at 5.21 MeV. The AMD calculation has predicted the presence of the parity doublet partner of the superdeformed band generated by the parity asymmetry. The  $K^\pi = 0^-$  band starting around 11 MeV in the negative parity (N3 in Fig. 13 (c)) is mainly composed of the wave function shown in Fig. 13 (d9) that also manifests  $^{12}\text{C}+^{28}\text{Si}$  clustering and can be understood as the parity doublet partner of the superdeformed band. The clustering nature of the superdeformed band also appears as the two excited molecular bands that are predicted at high excitation energy region (HN1 and HN2 in Fig. 13 (e)). These bands are dominated by the wave functions with  $N$  larger than for the superdeformed band dominated by (d4)-(d6), which indicates that they are the nodal excitation modes of the inter-cluster motion. Similar to the case of  $^{32}\text{S}$ , the superdeformed band (SD) and nodal excited bands (HN1 and HN2) can be understood as a series of the  $^{12}\text{C}+^{28}\text{Si}$  cluster bands. Thus,

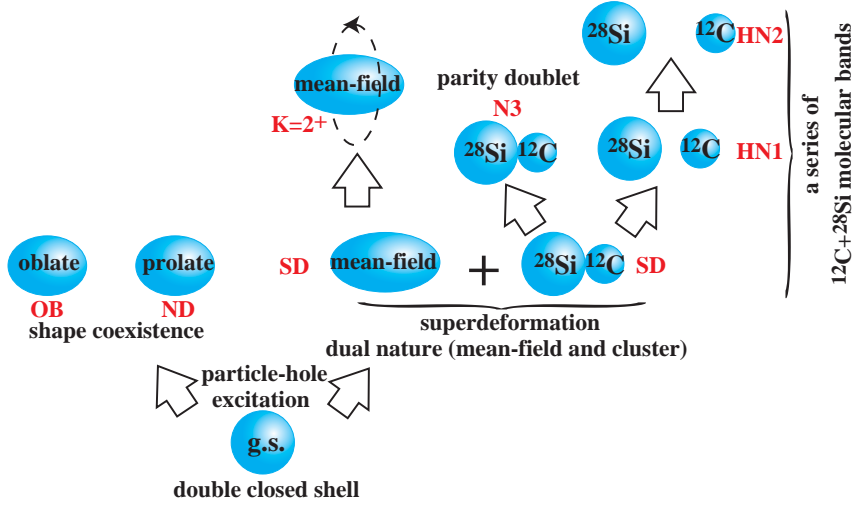


Fig. 14. Schematic figure summarizing the excitation modes of  $^{40}\text{Ca}$ . Prolate and oblate deformed states coexist at small excitation energy. The superdeformed band has dual nature of the mean-field and  $^{12}\text{C}+^{28}\text{Si}$  clustering. The triaxiality of the superdeformed band generates the  $K^\pi = 2^+$  sideband, while parity asymmetry of the  $^{12}\text{C} + ^{28}\text{Si}$  cluster structure generates the parity doublet partner. Furthermore, the nodal excitation of the inter-cluster motion generates a series of the  $^{12}\text{C} + ^{28}\text{Si}$  molecular bands.

the observation of the parity doublet partner and nodal excited bands will be essential to reveal clustering nature of the superdeformed band. It is also noted that the triaxial deformation of the superdeformed band has been also discussed in Ref. 124), and it has been suggested that the  $K^\pi = 2^+$  band accompanies the superdeformed band.

The situation of the  $^{40}\text{Ca}$  is schematically summarized as shown Fig. 14. Above the ground state, a prolate and oblate shape coexistence presents as two rotational bands. The superdeformed band is also located at the similar energy region and manifests the dual nature of the strongly deformed mean-field and  $^{12}\text{C}+^{28}\text{Si}$  clustering. The AMD calculation has predicted that the  $^{12}\text{C}+^{28}\text{Si}$  clustering nature of the superdeformed band generates the parity doublet partner in the negative-parity states from the parity asymmetry and the nodal excited bands at highly excited region from the excitation of the inter-cluster motion.

### 3.5. Decoupling between Proton and neutron deformations

For  $Z \neq N$  unstable nuclei, exotic phenomena concerning nuclear deformation have been discovered. If the shell effect for proton orbits and that for neutron ones compete with each other, the shape of proton density may be affected by the neutron structure, or it might be insensitive to neutron structure. In the latter case, decoupling of deformations between proton density and neutron one may occur. The decoupling, i.e., different proton and neutron deformations is possible in light-mass nuclei and it can be observed in the quadrupole transition properties such as the ratio of the neutron transition matrix amplitude to the proton one (so-called

$M_n/M_p$  ratio).

Such a decoupling between proton and neutron shapes has been suggested, for instance, in  $^{16}\text{C}$  for which an enhanced  $M_n/M_p$  ratio called neutron dominance has been observed in the ground-band transition,  $2_1^+ \rightarrow 0_1^+$ , in inelastic scattering.<sup>125)</sup> The neutron dominance was described by opposite deformations, i.e., an oblate proton shape and a prolate neutron one (Fig. 15) in the study with AMD.<sup>126),127)</sup> The opposite deformations in  $^{16}\text{C}$  has been supported also by the abnormally small  $E2$  transition strength  $B(E2; 2_1^+ \rightarrow 0_1^+) = 2.6 \pm 0.9 \text{ e}^2\text{fm}^4$  observed by the life time measurement of the  $^{16}\text{C}(2_1^+)$ .<sup>128)</sup> The strength  $B(E2; 2_1^+ \rightarrow 0_1^+)$  in  $^{16}\text{C}$  is small compared with those for other C isotopes,  $^{10}\text{C}$ ,  $^{12}\text{C}$ , and  $^{14}\text{C}$ . The hindrance of the  $B(E2; 2_1^+ \rightarrow 0_1^+)$  implies a small proton deformation, however, it seems to contradict a large deformation expected from the small excitation energy of the  $2_1^+$  state if proton and neutron deformations are assumed to be consistent as usual.

We studied the structure of even-even C isotopes with AMD.<sup>126),129)</sup> The systematics of the binding energies, radii, and  $E2$  transition strengths of C isotopes were qualitatively reproduced by a simple version of AMD calculations (VBP). The results indicate that the neutron shape drastically changes depending on the neutron number, while the proton shape is rather stable and insensitive to the neutron structure. One of the striking features is that the difference between proton and neutron shapes was suggested in  $^{16}\text{C}$  and  $^{10}\text{C}$  in which prolate neutron shapes are favored. In spite of the prolate neutron structure, the proton structure shows an oblate deformation resulting in the opposite deformations. The deformation parameters for proton and neutron densities of the intrinsic state are  $(\beta_p, \gamma_p) = (0.41, 0.27\pi)$  and  $(\beta_n, \gamma_n) = (0.53, 0.00\pi)$  for  $^{10}\text{C}$ , and they are  $(\beta_p, \gamma_p) = (0.32, 0.26\pi)$  and  $(\beta_n, \gamma_n) = (0.34, 0.00\pi)$  for  $^{16}\text{C}$  (Figs. 15 and 16). The reason for opposite proton and neutron deformations is that a  $Z = 6$  system favors an oblate proton shape because of the proton shell effect while a  $N = 10$  or  $N = 4$  nucleus has prolate trends of the neutron shape due to the neutron shell effect. In other words, the  $Z = 6$  proton structure is not so much affected by the neutron structure but it keeps the oblate tendency.

To discuss the neutron deformation, mirror analysis is useful. In the mirror analysis for  $^{10}\text{C}$  and  $^{10}\text{Be}$ , the neutron transition matrix  $M_n$  for the ground-band transition is evaluated from  $B(E2)$  in  $^{10}\text{Be}$  by assuming mirror symmetry. The experimental value of the  $M_n/M_p$  ratio in  $^{10}\text{C}$  deduced by the mirror analysis is described by the AMD calculation, and it can be understood with the opposite deformations between proton and neutron densities (Fig. 16). The neutron dominance in the ground-band transition is more remarkable in  $^{16}\text{C}$  as seen in the theoretical results. Unfortunately, there is no direct data of the  $E2$  strength for the mirror nuclei of  $^{16}\text{C}$ , however, as mentioned before, the observed inelastic scattering cross section implies an enhanced  $M_n/M_p$  ratio indicating the neutron dominance.<sup>125)</sup> It is worth to mention that microscopic coupled-channel calculations with the transition densities obtained by the AMD calculation have reproduced the inelastic scattering data successfully.<sup>127)</sup>

To clarify the oblate shape of the proton structure in  $^{16}\text{C}$  and  $^{10}\text{C}$ , observations of possible  $K = 2$  side bands and their transition properties would be helpful probes.

Such a nucleus having oblate proton and prolate neutron structures may show an isovector triaxiality. In the case, a  $K = 2$  side band can be constructed from the rotation around the symmetric axis of the prolate neutron part instead of the rotation around the perpendicular axis for the  $K = 0$  ground band (Fig. 16). Since the proton contribution should be dominant while the neutron contribution is minor in the rotation for the  $K = 2$  side band, the inter-band transition  $2_2^+ \rightarrow 0_1^+$  may show the proton dominance resulting in a small  $M_n/M_p$  ratio. In fact, the calculated  $M_n/M_p$  ratios for the  $2_2^+ \rightarrow 0_1^+$  in  $^{10}\text{C}$  and  $^{16}\text{C}$  are quenched and they indicate the proton dominance. There is no experimental information of the transition strength for  $2_2^+ \rightarrow 0_1^+$ . Inelastic scatterings of  $^{10}\text{C}$  and  $^{16}\text{C}$  will be good probes to experimentally confirm the proton dominance.

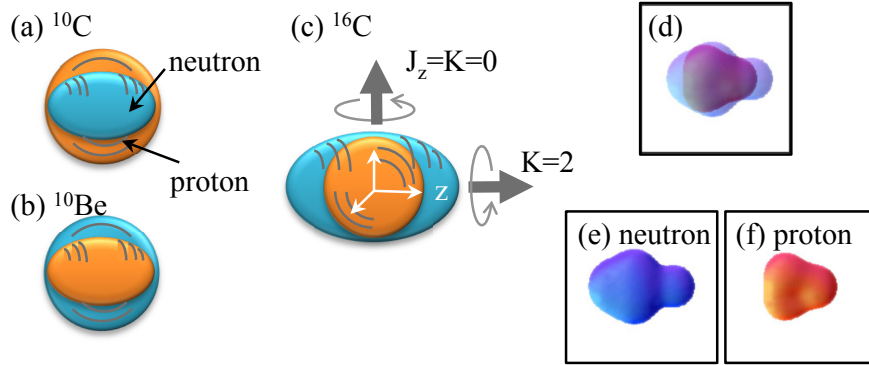


Fig. 15. Schematic figures for different shapes of proton and neutron densities in (a)  $^{10}\text{C}$ , (b)  $^{10}\text{Be}$ , and (c)  $^{16}\text{C}$ . (d) Surface cut at constant proton and neutron densities of  $^{16}\text{C}$  obtained by the VBP calculations with AMD. (e) Prolate neutron density of  $^{16}\text{C}$ . (f) Oblate proton density of  $^{16}\text{C}$ .

#### §4. Applications of time-dependent AMD method to nuclear response and reaction

Interesting phenomena, including clustering phenomena, appear in nuclear many-body systems not only near the ground state but also in excited states in wide range of excitation energies. These include giant resonances of collective modes and stronger expansion of the system which is often followed by the disintegration into fragment nuclei. Not only the collective degrees of freedom but also non-collective (thermal) excitations play important roles in many cases. Since the number of states increases very rapidly as the excitation energy goes up, it is difficult to describe these phe-

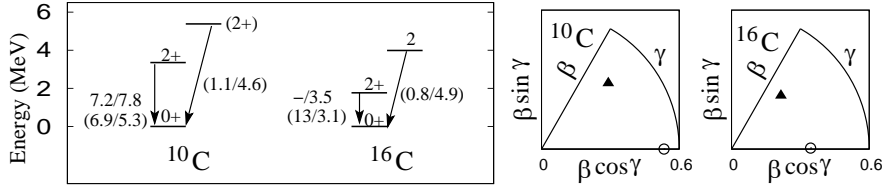


Fig. 16. Left: the experimental energy levels of the  $0_1^+$ ,  $2_1^+$ , and  $2_2^+$  states and  $M_n/M_p$  ratios for the  $2_1^+ \rightarrow 0_1^+$  and  $2_2^+ \rightarrow 0_1^+$  of  $^{10}\text{C}$  and  $^{16}\text{C}$ .<sup>130),128)</sup> The experimental values of the neutron matrix amplitude ( $M_n$ ) are deduced from the corresponding  $B(E2)$  values of the mirror nucleus. The values in the parentheses are the theoretical values for  $M_n/M_p$  of the AMD calculation.<sup>131)</sup> Right: deformation parameters for the intrinsic wave functions of  $^{10}\text{C}$  and  $^{16}\text{C}$ . The filled triangles indicate  $\beta_p$  and  $\gamma_p$  for the proton part and the open circles are  $\beta_n$  and  $\gamma_n$  for the neutron part.

nomena based on individual quantum states. The time-dependent version of AMD has been a powerful approach for such problems of highly excited systems.

#### 4.1. Dipole resonances

Among exotic phenomena in neutron-rich nuclei, one of the hot subjects is dipole strengths in low energy regions, which are expected to enhance in neutron-rich nuclei due to excess neutrons. For instance, soft resonances in extremely low-energy regions and pygmy resonances below giant dipole resonance (GDR) energy are attracting great interests (see, for example, Refs. 132), 133), 134), 135), 136), 137) and references therein). To investigate isovector dipole responses of neutron-rich nuclei, we applied a time-dependent version of AMD without stochastic terms.<sup>138)</sup>

In order to calculate responses to external fields, we first solve the static problem and obtain the optimum parameter set  $Z^0$ , which gives the energy minimum state  $\Phi_{\text{AMD}}(Z^0)$  in the AMD model space. Then, we boost the  $\Phi_{\text{AMD}}(Z^0)$  instantaneously at  $t = 0$  by imposing an external perturbative dipole field,

$$\Psi(t = 0+) = e^{-i\epsilon F} \Phi_{\text{AMD}}(Z^0), \quad (4.1)$$

$$V_{\text{ext}}(\mathbf{r}, t) = \epsilon F(\mathbf{r}) \delta(t), \quad (4.2)$$

$$F(\mathbf{r}) = \mathcal{M}(E1, \mu) = \sum_i^A e^{\text{rec}} r_i Y_{1\mu}(\hat{\mathbf{r}}_i), \quad (4.3)$$

where  $\epsilon$  is an arbitrary small number and  $e^{\text{rec}}$  is the  $E1$  recoil charge,  $Ne/A$  for protons and  $-Ze/A$  for neutrons. Note that the initial state  $\Psi(t = 0+)$  after imposing the dipole field is written with a single AMD wave function  $\Phi_{\text{AMD}}(Z(t = 0+))$ .

Following the time-dependent AMD method, we can calculate the time evolution of the system,  $\Psi(t) = \Phi_{\text{AMD}}(Z(t))$ , from the initial state  $\Psi(t = 0+)$  by using the equation of motion Eq. (2.5). Once the wave function  $\Psi(t)$  is obtained as a function of time, the transition strength can be obtained by Fourier transform of the expectation

value of  $\mathcal{M}(E1, \mu)$  as follows,

$$\frac{dB(\omega; E1, \mu)}{d\omega} \equiv \sum_n |\langle n | \mathcal{M}(E1, \mu) | 0 \rangle|^2 \delta(\omega - \omega_n) \quad (4.4)$$

$$= -\frac{1}{\pi\epsilon} \text{Im} \int_0^\infty dt \langle \Psi(t) | \mathcal{M}(E1, \mu) | \Psi(t) \rangle e^{i\omega t}, \quad (4.5)$$

where  $|0\rangle$  is the ground state and  $|n\rangle$  is the excited state with the excitation energy  $\hbar\omega_n$ .

In the present framework,  $dB(\omega; E1)/d\omega$  consists of discrete peaks in principle, because the present AMD method is a bound state approximation and continuum states are not taken into account. We introduce a smoothing parameter  $\Gamma$  by hand in the Fourier transform in Eq. (4.4) which may simulate the escape and spreading widths of resonances.

One of the advantages of time-dependent AMD is that we can obtain intuitive interpretations for each mode by analyzing time evolution of Gaussian centers  $\mathbf{Z}_i(t)$  of single-particle wave packets. Another advantage is that the present method is free from the spurious center-of-mass motion because center-of-mass motion can be exactly separated from  $\Psi(t)$ .

We applied this method to Be, B, and C isotopes and investigated the  $E1$  resonances.<sup>138)</sup> The  $E1$  strengths are shown in Fig. 17. It was found that remarkable peaks appear in  $^{10}\text{Be}$ ,  $^{15}\text{B}$ , and  $^{16}\text{C}$  in the  $E^* = 10 - 15$  MeV region decoupling from the GDR. Those soft dipole resonances arise from the relative motion of excess neutrons against a core, which is decoupled from the motion inside the core. In other words, the soft resonances appear due to the excitation of excess neutrons around the rather hard core. In fact, the strengths of the soft dipole resonances almost exhaust the cluster sum rule values for the core and valence neutrons. In further neutron-rich B and C isotopes with  $N > 10$ , the strengths for the soft dipole resonances decline compared with those in  $^{15}\text{B}$  and  $^{16}\text{C}$ . The reason for decreasing low-lying strengths is that motion of excess neutrons assimilates into neutron motion inside the core and its decoupling from the core weakens. As a result, the excitation energies of the GDR decrease with the enhancement of the neutron skin. It is striking that strengths of the soft dipole resonances do not necessarily increase with the increase of excess neutrons. Instead, the feature of the soft resonances rapidly changes depending on the proton and neutron numbers of the system. The strengths of the soft dipole resonances depends on how much the coherent motion of the excess neutrons decouples from the motion inside the core.

#### 4.2. Radial oscillations

Radial breathing oscillations of nuclei are interesting particularly because they are closely related to the compressibility of nuclei and nuclear matter. The AMD approach is, however, not very suitable for the precise analysis of the monopole strengths since the state boosted by the monopole operator from the ground state AMD wave function is no longer an AMD state. Nevertheless, AMD can be a powerful tool to explore the radial oscillations at various amplitudes. The large amplitude oscillations should be continuously linked to the expansion of nuclei without restora-

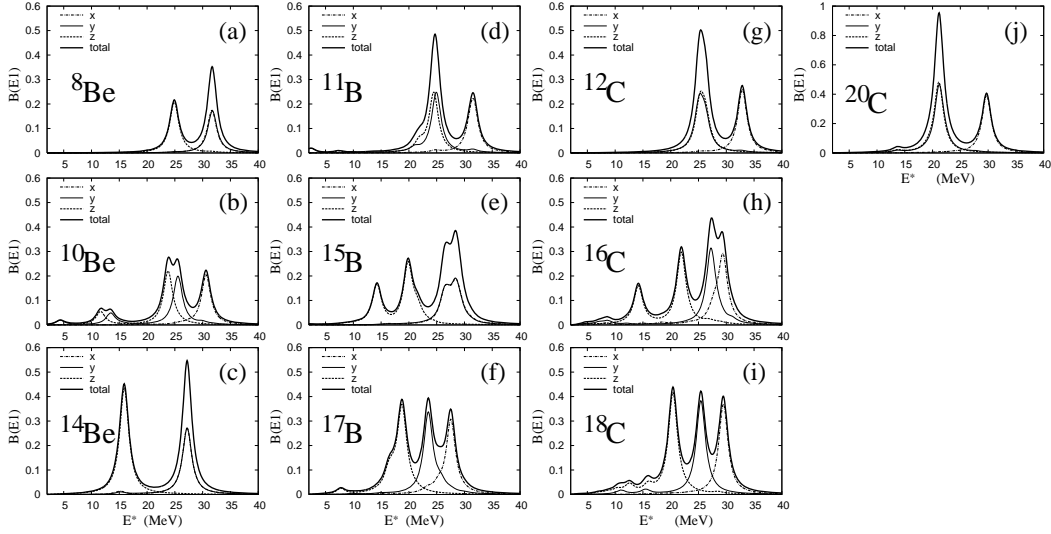


Fig. 17.  $E1$  transition strengths ( $e^2\text{fm}^2/\text{MeV}$ ) of Be, B, and C isotopes calculated with the time-dependent AMD method by using the MV1 ( $m = 0.576$  and  $b = h = 0$ ) + G3RS ( $u_I = -u_{II} = 900$  MeV) force.<sup>138)</sup> The smoothing parameter is chosen to be  $\Gamma = 2$  MeV. Thin dash-dotted, solid, and dotted lines are the contribution of vibration for the  $x, y$ , and  $z$ -directions, respectively. The total strengths are shown by the thick solid lines.

tion at higher energies where many-body correlations play important roles in forming clusters and fragment nuclei. Therefore the possibility of cluster correlations in lower energy oscillations is an interesting question.

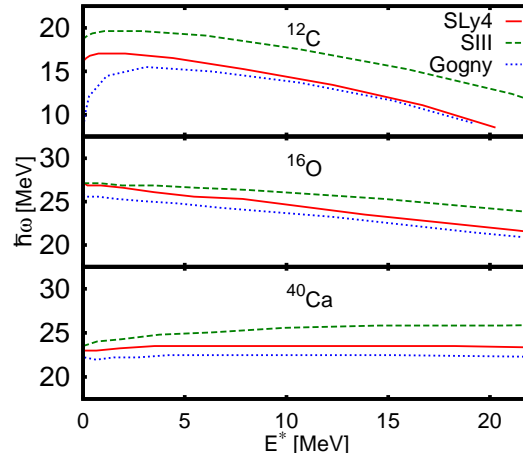


Fig. 18. AMD prediction for the frequency  $\hbar\omega$  of the radial oscillation as a function of the oscillation energy for  $^{12}\text{C}$ ,  $^{16}\text{O}$  and  $^{40}\text{Ca}$  with the SLy4, SIII and Gogny interactions. The nuclear matter incompressibilities for these interactions are  $K = 230, 355$  and  $228$  MeV, respectively. The figure is taken from Ref. 139).

The radial oscillations of the  $^{12}\text{C}$  and other nuclei were calculated with AMD [Eq.



(2·5)] without any stochastic terms in Ref. 139). The time evolution is solved from the initial state prepared by placing three  $\alpha$  clusters on a regular triangle in the  $^{12}\text{C}$  case. By changing the size of the initial regular triangle, oscillations with different amplitudes were studied. Figure 18 shows the dependence of the oscillation frequency on the amplitude or the excitation energy. The results for three different effective interactions are shown. Dependence on the incompressibility is clearly observed. The dependence on the amplitude suggests the unharmonicity of the oscillation. It should be noted that the one-phonon excitation corresponds to the excitation energy of  $E^* = \hbar\omega$  where  $\omega$  is the angular frequency.

The calculations of Fig. 18 were carried out with the width parameters  $\nu$  that optimize the ground state energy. Depending on the chosen width parameter, however, the frequency sometimes shows anomalous behavior as in the system of a double-well potential.<sup>139)</sup>

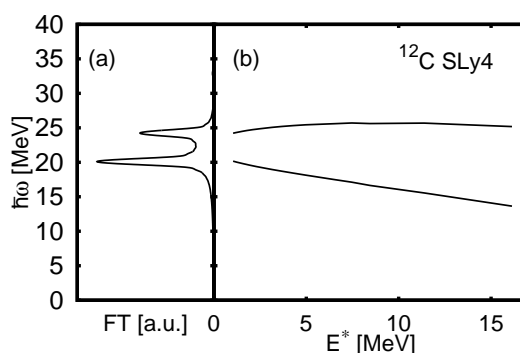


Fig. 19. (a) Fourier transform  $\text{FT}[r](\omega)$  of the FMD oscillation pattern in small amplitude, with the same initial condition as in the AMD calculation. (b) The peak position  $\hbar\omega$  as a function of the excitation energy. The figure is taken from Ref. 139).

The same problem was studied by the fermionic molecular dynamics (FMD) as well.<sup>139)</sup> In FMD, the width parameters  $\nu_i(t)$  of individual wave packets are treated as time-dependent variables as well as the centroid variables. In this case, the calculated result shows an oscillation pattern composed of two modes with different frequencies as shown in Fig. 19. By analyzing the motions of the variables, it was found that one of the two modes corresponds to the change of the wave packet widths and the other corresponds to the motion of the wave packet centroids. The latter mode is the same as that observed in the AMD result and related to the  $\alpha$ -clustering degrees of freedom. The former mode is the breathing of individual single-particle wave packets. Thus these calculations suggest that the single-particle excitation and the clustering excitation are both important in radially oscillating systems. The simplest version of AMD without any stochastic terms can describe clustering excitations.

#### 4.3. Multifragmentation in expanding systems

It has been well known experimentally that a lot of fragment nuclei are produced in each event of heavy-ion collisions in various situations if the incident en-

ergy is more than ten MeV/nucleon. Multifragmentation is an interesting problem in excited nuclear systems, in which quantum many-body correlations play essential roles as well as the existence of nuclear liquid-gas phase transition. The microscopic description of multifragmentation is, in principle, a highly complicated problem of quantum many-body systems. Transport models have been developed for heavy-ion collisions with some classical approximations. Compared with other transport models, some quantum features have been incorporated into AMD by employing fully antisymmetrized wave functions.

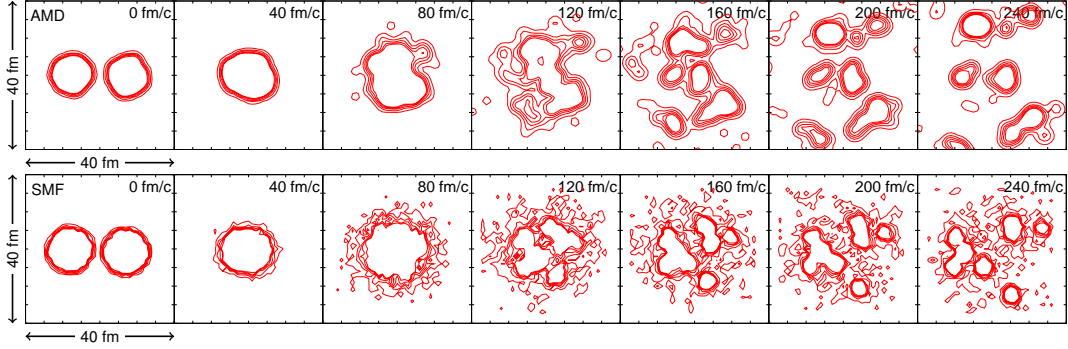


Fig. 20. Time evolution of density profiles obtained by the AMD (upper) and SMF (lower) models, for the central collision of  $^{112}\text{Sn} + ^{112}\text{Sn}$  at 50 MeV/nucleon.

Figure 20 shows a typical example of the time evolution of  $^{112}\text{Sn} + ^{112}\text{Sn}$  central collisions at 50 MeV/nucleon.<sup>140),141)</sup> The calculation by AMD in the upper row is compared with the calculation by the stochastic mean-field (SMF) model in the lower row. In both cases, the system compressed at an early stage starts to expand almost spherically. As the expansion proceeds, the density fluctuation develops to form many fragments.

The AMD calculation was performed with the coherence time  $\tau = \tau_{\text{NN}}$ . The SMF model, which is based on the single-particle motion in the mean field, takes into account the two-nucleon collisions and fluctuations.<sup>142)</sup> Therefore these two models are conceptually similar, but the results can be different due to the different approximate treatments of fluctuations. In fact, it is observed that the density fluctuation (among different events) is already developing in AMD at the relatively early stage of  $50 \lesssim t \lesssim 100$  fm/c, while the fluctuation develops in SMF only at a later stage  $t \sim 100$  fm/c suggesting a fragmentation mechanism by spinodal decomposition.<sup>143)</sup> Thus the many-body correlations are stronger in AMD. This difference can be interpreted as the origin of the differences in the expansion velocity, the nucleon emission and so on predicted by these models.<sup>140),141)</sup>

The final results of these models for the fragment charge distribution have been compared with the experimental data with reasonable successes.<sup>144),29)</sup> Figure 21 shows the AMD results compared with data. The result depends very much on the choice of the coherence time. In this reaction system, the fragment yields for  $Z \gtrsim 3$  are well reproduced by AMD when the wave packet splitting with the coherence time

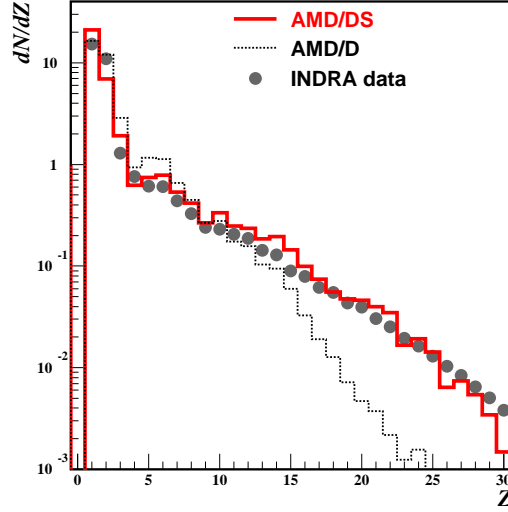


Fig. 21. The charge distribution of the produced clusters in  $^{129}\text{Xe}+\text{Sn}$  collisions at 50 MeV/nucleon with the impact parameter  $0 < b < 4$  fm, after calculating the secondary decay of excited clusters and applying the experimental filter for the detector setup. Solid histogram (labeled AMD/DS) shows the result of AMD with the coherence time  $\tau = \tau_{\text{NN}}$ , while the dotted histogram (labeled AMD/D) shows the result with the strongest decoherence  $\tau \rightarrow 0$ . The INDRA experimental data are shown by solid points. The figure is taken from Ref. 29).

$\tau = \tau_{\text{NN}}$  is introduced. It is often convenient to define the liquid and gas parts of the system as the parts composed of  $Z \geq 3$  fragments and  $Z \leq 2$  particles, respectively. The comparison shows that the total charge of the liquid part,  $Z_{\text{liq}}$ , in the AMD result (with  $\tau = \tau_{\text{NN}}$ ) is consistent with the experimental data, and therefore the total charge of the gas part,  $Z_{\text{gas}} = Z_{\text{system}} - Z_{\text{liq}}$ , is also consistent.

However, a problem is found in the composition of the gas part in the result with  $\tau = \tau_{\text{NN}}$ . The  $\alpha$ -particle multiplicity  $M_{\alpha} \approx 7$  is too small and the proton multiplicity  $M_p \approx 20$  is too large compared with the experimental data  $M_{\alpha} \approx M_p \approx 10$ . It should be noted that only about 10% of the total protons in the system is emitted as free protons in this reaction at 50 MeV/nucleon. It is also known experimentally that still a half of the protons are bound in clusters even at 1 GeV/nucleon.<sup>145)</sup> Thus the experimental data have been suggesting the importance of cluster correlations. The comparison with the data indicates that the AMD approach with the wave packet splitting, which is largely based on the single-particle motion in the mean field, does not include sufficient cluster correlations in the dynamics. The problem of the gas composition may influence on the liquid part of the system because the energy balance and the number of the effective degrees of freedom will change as the gas composition changes. Therefore the proper treatment of cluster correlations in dynamical approaches is an urgent issue.

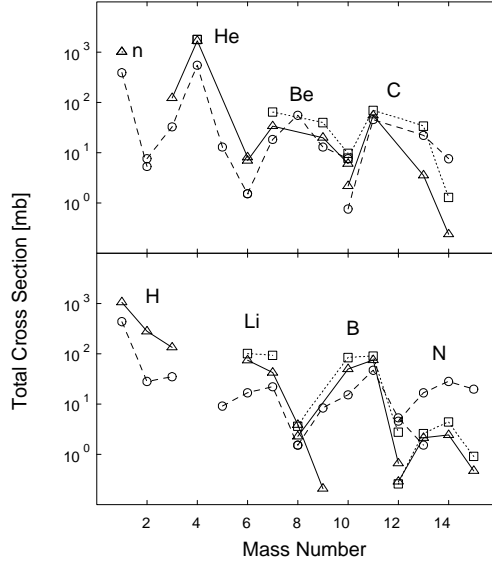


Fig. 22. Isotope distribution in  $^{12}\text{C} + ^{12}\text{C}$  reaction at 28.7 MeV/nucleon. Circles are the yields before the secondary decay, while triangles are those after the secondary decay. Squares are the experimental data. Lines connect isotopes. The figure is taken from Ref. 2).

#### 4.4. Fragmentation in collisions of light nuclei

In an early study with AMD, the fragmentation in the  $^{12}\text{C} + ^{12}\text{C}$  reaction was studied at 28.7 MeV/nucleon.<sup>1),2)</sup> The fragment isotope distribution is reproduced well by AMD as shown in Fig. 22. Especially the large production cross section of  $\alpha$  particles is well reproduced in this case. The calculation was done with the stochastic two-nucleon collisions but without wave packet splitting. Thus the situation here is different from the multifragmentation in heavier systems as seen in the previous subsection where the wave packet splitting is very important.

The detailed mechanism of the fragmentation of the  $^{12}\text{C}$  projectile was studied in Ref. 146) by Takemoto *et al.* The solid line of the lower part of Fig. 23 shows the distribution of the excitation energy of the  $^{12}\text{C}$  projectile after the interaction with the target in  $^{12}\text{C} + ^{14}\text{N}$  reaction at 35 MeV/nucleon. In addition to the big bump around  $E^* \sim 30$  MeV, there is a sharp peak at  $E^* \sim 10$  MeV. The  $\alpha$ -clustering states of  $^{12}\text{C}$  in this energy region are strongly excited by the heavy-ion reaction, and they contribute to the large yield of  $\alpha$  particles. In fact, the dashed line shows the contribution from the events where  $^{12}\text{C}$  broke up into three  $\alpha$  particles. On the other hand, in the proton induced reactions, the excitation of  $^{12}\text{C}$  is mainly of single particle nature and the  $\alpha$  clustering states are not excited at all as shown in the upper part of Fig. 23.

For the multifragmentation in  $^{40}\text{Ca} + ^{40}\text{Ca}$  collisions at 35 MeV/nucleon, the wave packet splitting plays important roles to enable the breakup of the system into small pieces. Figure 24 compares the results without wave packet splitting and with the wave packet splitting in the limit of the small coherence time  $\tau \rightarrow 0$  (i.e., the

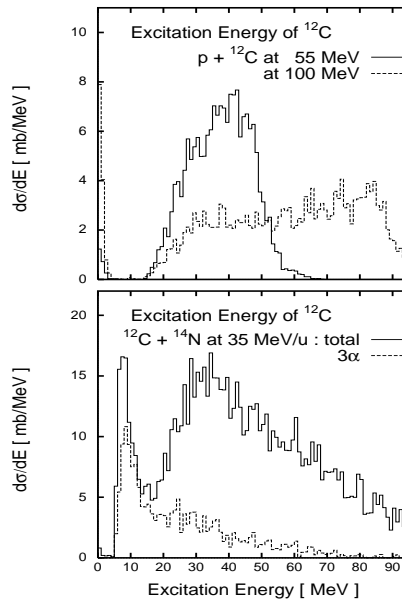


Fig. 23. The distribution of excitation energy of  $^{12}\text{C}$  projectile before its breakup. Upper figure is for  $p + ^{12}\text{C}$  collisions, while the lower figure is for  $^{12}\text{C} + ^{14}\text{N}$  collision at 35 MeV/nucleon. The figure is taken from Ref. 146).

strongest decoherence). The latter result is consistent with the experimental data. Without wave packet splitting, the two nuclei go through each other without forming fragments of intermediate size. The wave packet splitting allows the mixing of the two nuclei or the neck formation, so that more than two fragments can be formed from the system expanding in the beam direction. The  $\alpha$ -particle multiplicity also depends on the wave packet splitting very much.

In short, the strength of the wave packet splitting (viewed from AMD) or the decoherence of the single-particle states (viewed from the mean-field theory) is a key ingredient for the description of fragmentation. For the stronger splitting, the system tends to expand strongly and to break into small fragments and many  $\alpha$  particles. Unfortunately, the appropriate strength seems to depend on the size of the system and/or the incident energy. A more consistent understanding may be possible if the cluster correlations in dynamical systems are more explicitly treated.

#### 4.5. Statistical properties of excited systems

One of the aims of the study of multifragmentation has been to extract the information of excited nuclear matter in which the liquid-gas phase transition is expected as in the system of the Van der Waals equation of state. The concept of phase transition in finite many-body systems, as in the heavy-ion collision systems, has been improved very much in recent studies.<sup>147),148)</sup> Phase transition is clearly defined in finite systems by considering microcanonical ensembles.

By solving the time evolution of a many-body system in a container of a finite

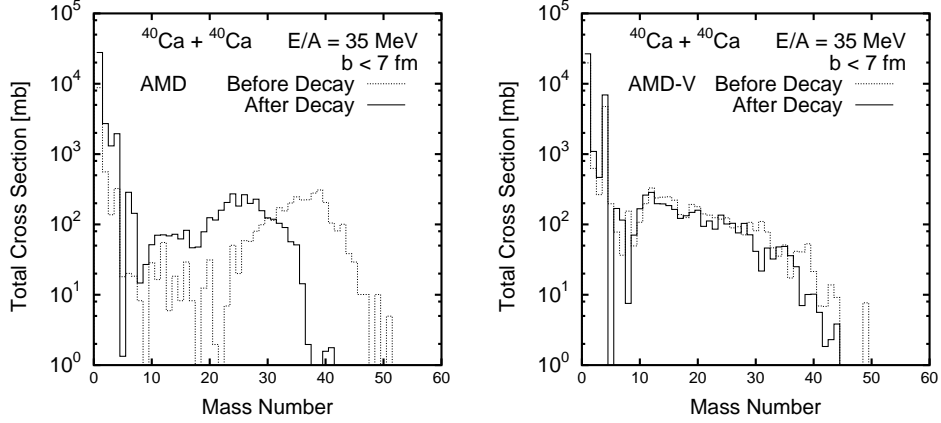


Fig. 24. Mass distribution in  $^{40}\text{Ca} + ^{40}\text{Ca}$  collision at 35 MeV/nucleon. Calculated results of AMD before and after the secondary decay are shown by dotted and solid histograms, respectively. The left figure is the result by AMD without wave packet splitting, and the right figure is the result with the strongest decoherence  $\tau \rightarrow 0$ . The figure is taken from Ref. 28).

volume for a very long time, it is possible in principle to generate a microcanonical ensemble for the given energy and volume. However, it is a non-trivial question whether dynamical models such as AMD can produce a correct statistical ensemble. In fact, the introduction of wave packet splitting into AMD was first motivated for the purpose to get a proper statistical properties with the fermionic caloric curve  $E^* = aT^2$  at low temperature.<sup>149),150)</sup> From a different point of view, Ohnishi and Randrup also introduced stochastic terms into molecular dynamics for quantum statistics.<sup>151)</sup> The caloric curves in the region of liquid gas phase transition was calculated by Sugawa and Horiuchi by employing AMD with an implementation of wave packet splitting.<sup>152),154)</sup> Fermionic molecular dynamics was also applied to the caloric curves.<sup>153)</sup> The caloric curves obtained in these studies were drawn under the condition of fixed volumes or for a system under a confining potential.

More recently, in Refs. 155), 156), Furuta and Ono performed AMD calculation to obtain constant-pressure caloric curves in which phase transition should be clearly identified. Wave packet splitting was considered with a density-dependent coherence time  $\tau(\rho)$  in this study. For a calculated microcanonical ensemble of a given energy  $E$  and a volume  $V$ , the temperature  $T$  is defined by using the kinetic energies of gas-like nucleons. The pressure  $P$  is obtained from the information of the reflections of particles at the boundary of the container. Then caloric curves are drawn as  $T(E)$  for different values of  $P$ . The result for the system of  $N = 18$  and  $Z = 18$  is shown in Fig. 25. Nuclear liquid-gas phase transition, as a first order phase transition, is clearly seen in this result as the back-bending of caloric curves.

The construction of microcanonical ensembles can also be regarded as a way to explore the many-body states at various excitation energies, as illustrated in Fig. 26. Above the ground state and low-lying excited states of the nucleus, there should be quite a lot of states which are characterized by the density of states  $W(E)$ . The

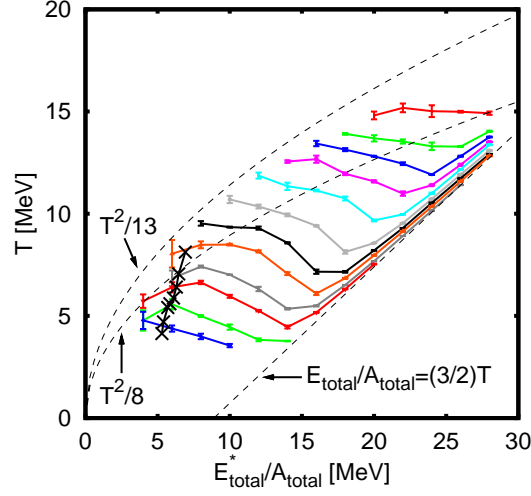


Fig. 25. Constant pressure caloric curves calculated with AMD for the  $A = 36$  system. The cross symbols indicate the equilibrium state corresponding to the reaction system from  $t = 80$  to  $300$  fm/c for  $^{40}\text{Ca} + ^{40}\text{Ca}$  central collisions. The figure is taken from Ref. 156).

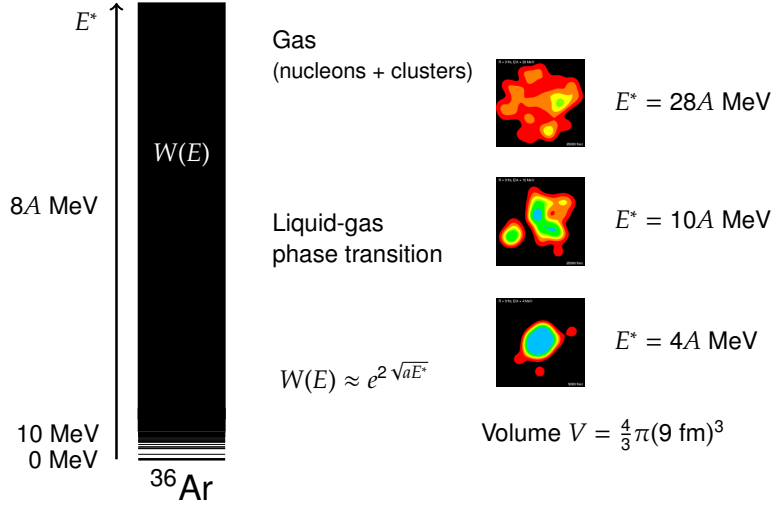


Fig. 26. Excited states of a many-nucleon system with  $N = Z = 18$  confined in a virtual spherical container with a radius of 9 fm. The density distribution at each excitation energy ( $E^*/A = 4, 10$  and 28 MeV) shows a snapshot taken from the AMD equilibrium calculation of Ref. 155).

density profile at each of the excitation energies  $E^*/A = 4, 10$  and 28 MeV is a sample taken from the calculated microcanonical ensemble.<sup>155)</sup> At low excitation energies, a single large nucleus is usually observed. The energy  $E^*/A = 10$  MeV is in the region of liquid-gas phase transition where  $W(E)$  shows an anomalous behavior and each density profile typically shows several nuclei being related to multifragmentation. It should be noted that the system confined in a container does not become a gas of

nucleons even though the excitation energy is higher than the binding energy of the nucleus. When the energy is further raised to 28 MeV/nucleon, for example, the state may be regarded as a gas state but the gas is composed of clusters as well as nucleons.

Thus it is now a great advantage of AMD that it can describe both dynamical reactions in heavy-ion collisions and virtually equilibrated systems reasonably well. In Ref. 156), we investigated the question whether equilibrium is really relevant in multifragmentation by comparing the details of reaction calculations and equilibrium calculations performed by the same AMD model. The calculations show that there exists an equilibrium ensemble which well reproduces the reaction ensemble at each reaction time  $t$  for the investigated period  $80 \leq t \leq 300$  fm/ $c$  in  $^{40}\text{Ca} + ^{40}\text{Ca}$  central collisions at 35 MeV/nucleon, as far as fragment observables (fragment yields and excitation energies) are concerned. Thus the corresponding temperature and excitation energy (or the volume and pressure) can be identified at each reaction time. In Fig. 25, the path of the reaction from  $t = 80$  to 300 fm/ $c$  is drawn by the cross symbols on the caloric curve figure. It is also important to note that there are some other observables which show discrepancies between the reaction and equilibrium ensembles.<sup>156)</sup> These may be interpreted as dynamical effects in the reaction. In particular, the usual static equilibrium at each instant is not realized since any equilibrium ensemble with the same volume as that of the reaction system cannot reproduce the fragment observables.

#### 4.6. *Symmetry energy effects in heavy-ion collisions*

The AMD simulations for heavy-ion collisions are useful not only to explain the experimental data but also to know what kind of information is reflected in the fragment formation. In particular, as demonstrated in the previous subsection, we may expect that statistical properties such as the equation of state can be extracted from the fragment observables even in dynamical collisions.

In heavy-ion collisions with unbalanced neutron and proton numbers, the difference between the neutron and proton motions is an interesting new degrees of freedom. The difference of flow pattern between neutrons and protons has been predicted to be sensitive to the density dependence of symmetry energy. From the viewpoint of liquid-gas phase transition, neutron-rich systems are quite interesting because new characters as two-component systems are expected. Namely, the gas part of the system is more neutron-rich than the liquid part, which can be called fractionation or distillation. This effect of isospin fractionation/distillation should be observable in the neutron-to-proton ratio of produced fragments.

In Refs. 158), 159), the fragment yields were analyzed in the AMD simulations for multifragmentation reactions of the central collisions of Ca isotopes at 35 MeV/nucleon, in order to see how the fragment isospin composition is related to the symmetry energy term of the effective interaction adopted in the calculation. For the fragment yields  $Y_i(N, Z)$  in the reaction  $i$  at  $t = 300$  fm/ $c$ , it was found that the isoscaling relation

$$Y_j(N, Z)/Y_i(N, Z) \propto e^{\alpha_{ij}N + \beta_{ij}Z} \quad (4.6)$$



is satisfied for any two reaction systems  $i$  and  $j$  which are different in the proton-to-neutron ratios. Isoscaling is expected under an equilibrium assumption and has been observed in the experimental data.<sup>157)</sup> Isoscaling is equivalent to the statement that the fragment yields are expressed as

$$Y_i(N, Z) = \exp[-K(N, Z) + \alpha_i N + \beta_i Z + \gamma_i] \quad (4.7)$$

by using a function  $K(N, Z)$  that is independent of the reaction system  $i$ . If the equilibrium is relevant to the reaction,  $K(N, Z)$  should contain a term  $(C_{\text{sym}}/T)(N - Z)^2/(N + Z)$ , where  $C_{\text{sym}}$  is a kind of symmetry energy which may depend on  $A$  or  $Z$  in principle. Based on this assumption, the isoscaling parameter is related to the symmetry energy by

$$\alpha_{ij} = \frac{4C_{\text{sym}}}{T} \left[ (Z/\bar{A}_i(Z))^2 - (Z/\bar{A}_j(Z))^2 \right], \quad (4.8)$$

where  $Z/\bar{A}_i(Z)$  represents the mean isospin asymmetry of the fragments for each given  $Z$  in the reaction  $i$ .

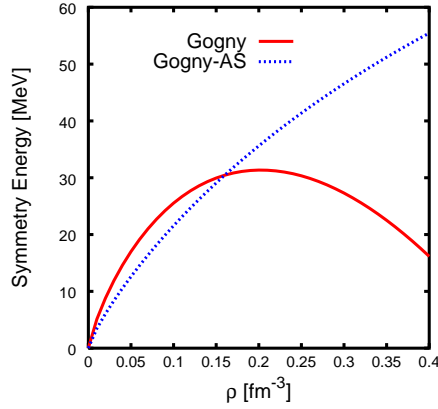


Fig. 27. Density dependence of the symmetry energy of nuclear matter for the Gogny force (solid line) and for the Gogny-AS force (dashed line).

AMD calculations were carried out with the Gogny force and the Gogny-AS force which are different in the density dependence of the symmetry energy as shown in Fig. 27. The result shows that the isoscaling parameter  $\alpha$  actually depends on the density dependence of the symmetry energy as shown in Fig. 28.<sup>158)</sup> Furthermore, the value of  $C_{\text{sym}}/T$  extracted from the simulation result is found to be almost independent of the fragment size  $A$  or  $Z$ ,<sup>159)</sup> which suggests that bulk properties are reflected in the fragment isotope yields rather than the symmetry energy for the ground state binding energies that depends on  $A$  due to the surface effect. To explain the obtained result,  $C_{\text{sym}}$  is identified with the bulk symmetry energy at about  $\frac{1}{2}\rho_0$ , with  $\rho_0$  being the saturation density of nuclear matter, and the temperature should be  $T \approx 3.4$  MeV. These values of the density and the temperature are reasonable as the condition for fragmentation.

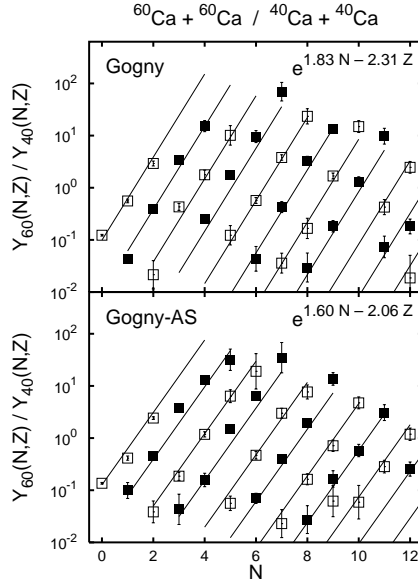


Fig. 28. The fragment yield ratio between the AMD simulations of central  $^{60}\text{Ca} + ^{60}\text{Ca}$  and  $^{40}\text{Ca} + ^{40}\text{Ca}$  collisions at 35 MeV/nucleon, at time  $t = 300$  fm/c. The top and bottom panels show, respectively, the results obtained using the Gogny and Gogny-AS forces. The extracted isoscaling parameters are  $\alpha = 1.82 \pm 0.06$  and  $\beta = -2.23 \pm 0.08$  for the Gogny force, and  $\alpha = 1.64 \pm 0.05$  and  $\beta = -2.09 \pm 0.07$  for the Gogny-AS force. The figure is taken from Ref. 158).

It should be noted that the above analysis has been done for the fragment yields at  $t = 300$  fm/c. In order to compare with experimental data, the effects of the decay of these primary fragments should be carefully considered.

## §5. Summary and perspective

In nuclear systems, cluster aspect is one of the essential features as well as mean-field aspect. Coexistence of cluster and mean-field aspects brings a variety of phenomena as functions of excitation energy and isospin degrees of freedom. For usual theoretical models, it is not easy to describe both behaviors of independent single nucleons in a mean field and spatially correlating nucleons in clusters. The AMD method is one of the theoretical approaches that can describe those two kinds of nature. In AMD, single-particle wave functions are written by localized Gaussian wave packets whose dynamics expresses assembling and disassembling of nucleons. The method has been applied to investigate nuclear reactions and structures and it has been proved to successfully describe a variety of phenomena in general nuclei.

In this paper, we reviewed the AMD approach and its application to nuclear structure and reaction studies. To show applicability of AMD some topics studied with time-independent and time-dependent versions of AMD were explained. In the applications of time-independent AMD to nuclear structure studies, structures

of neutron-rich nuclei such as Be, C, F, Ne, and Mg isotopes were described focusing on cluster aspects. The results suggested a variety of structures appear in unstable nuclei as well as in stable nuclei. Deformation and cluster phenomena in  $Z \sim N$  nuclei in  $p$ - and  $sd$ - shell regions were also described. The applications of time-dependent AMD contain various topics such as fragmentation in heavy-ion collisions, nuclear responses and virtual systems in thermal equilibrium. AMD calculations successfully described multifragmentation which is one of the remarkable phenomena in heavy-ion collisions. Comparisons with predictions by other models and/or experimental data suggest the important balance between the single-particle motions and the many-body correlations to form clusters and fragments in these phenomena. The AMD approach is suited to link the reaction observables to the equilibrium properties of nuclear matter such as liquid-gas phase transition and the equation of state of asymmetric nuclear matter.

Success of those studies using the AMD approach greatly owes to characteristics of the AMD model, for instance, advantages listed below.

- It is able to describe cluster and mean-field aspects without assuming existence of clusters nor mean fields.
- It is applicable to both static and dynamical problems.
- It is applicable to general nuclei with given proton and neutron numbers.
- Center-of-mass motion can be exactly extracted.

In addition to the above advantages, the model can be easily extended because of flexibility of AMD wave functions. For instance, parity and angular-momentum projections and superposition of wave functions are performed in structure calculations, and stochastic collisions are incorporated in calculations of heavy-ion collisions.

Present structure studies with the AMD method cover light-mass regions of nuclear chart up to  $pf$ -shell nuclei. It is a future problem to apply the method to further heavy-mass regions and progress systematic studies covering wide regions of the nuclear chart.

Origins of cluster formation and breaking should be clarified from the point of view of nuclear force. Unfortunately, the present AMD framework is model calculation and it requires phenomenological effective nuclear interactions. To calculate nuclear systems based on realistic nuclear forces is one of the important issues in nuclear physics. In fact, there are many attempts of *ab initio* calculations though practical *ab initio* calculations are still limited in very light systems. For systematic study covering a wide mass number region, model calculations are efficient. To achieve model calculations starting from realistic nuclear forces a main problem is how to deal with complicated many-body correlations. One of the promising methods is the unitary correlation operator method (UCOM)<sup>160),161),162)</sup> recently proposed to incorporate efficiently short-range and tensor correlations in structure models such as FMD. To understand nuclear structure from fundamental point of view, more sophisticated versions of the AMD method would be required.

Another issue of the AMD approach would be wide application to reaction phenomena. Although the AMD method has been extensively applied to violent reactions above ten MeV/nucleon, its applications to lower-energy reaction phenomena are limited. Motivated by recent progress of experimental studies, low-energy re-

actions such as resonances, fusion/capture, and transfer reactions are interesting problems to be solved concerning cluster phenomena in unstable nuclei.

### Acknowledgments

We would like to thank A. Dote, T. Furuta, N. Furutachi, H. Horiuchi, T. Suhara, and Y. Taniguchi, for fruitful discussions and collaborations. Parts of numerical calculations of this work were performed by using supercomputers at RCNP in Osaka University, those in High Energy Accelerator Research Organization, and those at YITP in Kyoto university. This work was supported by Grant-in-Aid for Scientific Research from Japan Society for the Promotion of Science (No. 21540253, No. 22540275).

### References

- 1) A. Ono, H. Horiuchi, T. Maruyama and A. Ohnishi, *Phys. Rev. Lett.* **68** (1992) 2898.
- 2) A. Ono, H. Horiuchi, T. Maruyama and A. Ohnishi, *Prog. Theor. Phys.* **87** (1992) 1185.
- 3) Y. Kanada-En'yo and H. Horiuchi, *Prog. Theor. Phys.* **93** (1995) 115; Y. Kanada-En'yo, H. Horiuchi and A. Ono, *Phys. Rev. C* **52** (1995) 628; Y. Kanada-En'yo and H. Horiuchi, *Phys. Rev. C* **52** (1995) 647.
- 4) A. Ono and H. Horiuchi, *Prog. Part. Nucl. Phys.* **53** (2004) 501.
- 5) Y. Kanada-En'yo and H. Horiuchi, *Prog. Theor. Phys. Suppl.* **142** (2001) 205.
- 6) Y. Kanada-En'yo M. Kimura and H. Horiuchi, *C. R. Physique* **4** (2003) 497.
- 7) Y. Kanada-En'yo and M. Kimura, *Lecture notes in physics* **818** (2010) 129.
- 8) A. Ono, *Phys. Rev. C* **59** (1999) 853.
- 9) M. Kimura and H. Horiuchi, *Nucl. Phys. A* **767** (2006) 58.
- 10) Y. Kanada-En'yo, *Phys. Rev. Lett.* **81** (1998) 5291.
- 11) K. Ikeda, N. Takigawa, H. Horiuchi, *Prog. Theor. Phys. Suppl.*, extra number (1968) 464.
- 12) H. Feldmeier, *Nucl. Phys. A* **515** (1990) 147.
- 13) H. Feldmeier, K. Bieler and J. Schnack, *Nucl. Phys. A* **586** (1995) 493.
- 14) A. B. Volkov, *Nucl. Phys.* **74** (1965) 33.
- 15) N. Yamaguchi, T. Kasahara, S. Nagata and Y. Akaishi, *Prog. Theor. Phys.* **62** (1979) 1018; R. Tamagaki, *Prog. Theor. Phys.* **39** (1968) 91.
- 16) J. Decharge and D. Gogny, *Phys. Rev. C* **21** (1980) 1568.
- 17) J. F. Berger, M. Girod and D. Gogny, *Comp. Phys. Commu.* **63** (1991) 365.
- 18) M. Beiner, H. Flocard, Nguyen van giai and P. Quentin, *Nucl. Phys. A* **238** (1975) 29.
- 19) E. Chabanat, P. Bonche, P. Haensel, J. Meyer and R. Schaeffer, *Nucl. Phys. A* **635** (1998) 231; *Erratum Nucl. Phys. A* **643** (1998) 441.
- 20) T. Ando, K. Ikeda and A. Tohsaki, *Prog. Theory. Phys.* **64** (1980) 1608.
- 21) N. Itagaki, S. Aoyama, *Phys. Rev.* **C61** (2000) 024303.
- 22) M. Kimura and H. Horiuchi, *Prog. Theor. Phys.* **107** (2002) 33.
- 23) M. Kimura, *Phys. Rev.* **C69** (2004) 044319.
- 24) T. Suhara and Y. Kanada-En'yo, *Prog. Theor. Phys.* **123** (2010) 303.
- 25) S. Aoyama, N. Itagaki and M. Oi, *Phys. Rev. C* **74**, 017307 (2006).
- 26) A. Doté, Y. Kanada-En'yo, H. Horiuchi, Y. Akaishi and K. Ikeda, *Prog. Theor. Phys.* **115** (2006) 1069.
- 27) N. Furutachi, M. Kimura, A. Doté and Y. Kanada-En'yo, *Prog. Theor. Phys.* **122** (2009) 865.
- 28) A. Ono and H. Horiuchi, *Phys. Rev. C* **53** (1996) 2958.
- 29) A. Ono, S. Hudan, A. Chbihi, J. D. Frankland, *Phys. Rev. C* **66** (2002) 014603.
- 30) M. Seya, M. Kohno, and S. Nagata, *Prog. Theor. Phys.* **65** (1981) 204.
- 31) W. von Oertzen, *Z. Phys. A* **354**, 37 (1996); **357** (1997) 355.
- 32) W. von Oertzen, *Nuovo Cimento* **110**(1997) 895 ; W. von Oertzen, *Eur. Phys. J. A* **11** (1997) 403.
- 33) N. Itagaki and S. Okabe, *Phys. Rev. C* **61** (1999) 044306 ; N. Itagaki, S. Okabe and K.

- Ikeda, Phys. Rev. C **62** (2000) 034301.
- 34) A. Doté, H. Horiuchi, and Y. Kanada-En'yo, Phys. Rev. C **56** (1997) 1844.
  - 35) M. Ito, K. Kato and K. Ikeda, Phys. Lett. **B588** (2004) 43.
  - 36) W. von Oertzen, M. Freer and Y. Kanada-En'yo, Phys. Rep. **432** (2006) 43.
  - 37) P. Descouvemont and D. Baye, Phys. Lett. **B505** (2001) 71.
  - 38) Y. Kanada-En'yo and H. Horiuchi, Phys. Rev. C **68** (2002) 014319.
  - 39) M. Ito, N. Itagaki, H. Sakurai and K. Ikeda, Phys. Rev. Lett. **100** (2008) 182502.
  - 40) M. Kimura, Phys. Rev. C **75** (2007) 034312.
  - 41) S. Okabe, Y. Abe, and H. Tanaka, Prog. Theory. Phys. **57** (1977) 866; S. Okabe and Y. Abe, Prog. Theor. Phys. **59** (1978) 315; S. Okabe, Y. Abe, Prog. Theory. Phys. **61** (1979) 1049.
  - 42) M. Kimura and N. Furutachi, Phys. Rev. C **83** (2011) 044304.
  - 43) Y. Ogawa, K. Arai, Y. Suzuki and K. Varga, Nucl. Phys. A **673** (2000) 122.
  - 44) K. Arai, Y. Ogawa, Y. Suzuki, and K. Varga, Prog. Theor. Phys. Suppl. **142** (2001) 97.
  - 45) P. Descouvemont, Nucl. Phys. A **699** (2002) 463.
  - 46) Y. Kanada-En'yo, H. Horiuchi and A. Doté, Phys. Rev. C **60** (1999) 064304.
  - 47) Y. Kanada-En'yo and H. Horiuchi, Phys. Rev. C **66** (2002) 024305.
  - 48) T. Suzuki and T. Otsuka, Phys. Rev. C **56**, 847 (1997).
  - 49) M. Freer, *et al.*, Phys. Rev. Lett. **82** (1999) 1383 ; M. Freer, *et al.*, Phys. Rev. C **63** (2001) 034301.
  - 50) A. Saito, *et al.*, Nucl. Phys. A **738** (2004) 337.
  - 51) M. Ito and Y. Sakuragi, Phys. Rev. C **62** (2000) 064310.
  - 52) Y. Fujiwara *et al.*, Prog. Theor. Phys. Suppl. **68** (1980) 29.
  - 53) A. Tohsaki, H. Horiuchi, P. Schuck, and G. Röpke, *Phys. Rev. Lett.* **87** (2001) 192501.
  - 54) Y. Funaki, A. Tohsaki, H. Horiuchi, P. Schuck and G. Röpke, Phys. Rev. C **67** (2003) 051306.
  - 55) G. Röpke, A. Schnell, P. Schuck, and P. Nozieres, Phys. Rev. Lett. **80** (1998) 3177.
  - 56) H. Morinaga, Phys. Rev. **101** (1956) 1956; Phys. Lett. **21**(1966) 78.
  - 57) Y. Kanada-En'yo, Prog. Theor. Phys. **117** (2007) 655.
  - 58) Y. Kanada-En'yo, Phys. Rev. C **75** (2007) 024302.
  - 59) T. Suhara and Y. Kanada-En'yo, Phys. Rev. C **82** (2010) 044301.
  - 60) M. Chernykh, H. Feldmeier, T. Neff, P. von Neumann-Cosel and A. Richter, Phys. Rev. Lett. **98** (2007) 032501.
  - 61) Y. Fukushima and M. Kamimura, *Proc. Int. Conf. on Nuclear Structure, Tokyo, 1977, edited by T. Marumori*, J. Phys. Soc. Jpn. **44** (1978) 225; M. Kamimura, Nucl. Phys. A **351** (1981) 456.
  - 62) E. Uegaki, S. Okabe, Y. Abe and H. Tanaka, Prog. Theor. Phys. **57** (1977) 1262. E. Uegaki, Y. Abe, S. Okabe and H. Tanaka, Prog. Theor. Phys. **59** (1978) 1031; **62** (1979) 1621.
  - 63) T. Kawabata *et al.*, *Phys. Lett.* **B646** (2007) 6.
  - 64) T. Yamada and Y. Funaki, Phys. Rev. C **82** (2010) 064315.
  - 65) D. Price *et al.*, Phys. Rev. C **75** (2007) 014305.
  - 66) P. J. Haigh *et al.*, Phys. Rev. C **78** (2008) 014319.
  - 67) T. Suhara, *private communications*.
  - 68) E. K. Warburton, J. A. Bechker and B. A. Brown, Phys. Rev. C **41** (1990) 1147 .
  - 69) C. Thibault *et al.*, Phys. Rev. C **12** (1975) 644.
  - 70) G. Huber *et al.*, Phys. Rev. C **18** (1978) 2342.
  - 71) T. Motobayashi *et al.*, Phys. Lett. **B346** (1995) 9.
  - 72) A. Poves and J. Retamosa, Phys. Lett. **B184** (1986) 311.
  - 73) N. Fukunishi, T. Otsuka and T. Sebe, Phys. Lett. **B296** (1992) 279.
  - 74) Y. Utsuno, T. Otsuka, T. Mizusaki and M. Honma, Phys. Rev. C **60** (1999) 054315.
  - 75) S. Takeuchi *et al.*, Phys. Rev. C **79** (2009) 054319.
  - 76) W. Schwerdtfeger *et al.*, Phys. Rev. Lett. **103** (2009) 012501.
  - 77) Z. M. Wang *et al.*, Phys. Rev. C **81** (2010) 064301.
  - 78) K. Wimmer *et al.*, Phys. Rev. Lett. **105** (2010) 252501.
  - 79) M. Kimura and H. Horiuchi, Prog. Theor. Phys. **107** (2002) 33.
  - 80) M. Kimura and H. Horiuchi, Prog. Theor. Phys. **111** (2004) 841.
  - 81) M. Kimura, Phys. Rev. C **75** (2007) 0413012.
  - 82) M. Kimura, arXiv:1105.3281v1

- 83) G. Neyens, Phys. Rev. C **84** (2011) 064310.
- 84) G. Neyens *et al.*, Phys. Rev. Lett. **94** (2005) 022501.
- 85) G. Klotz *et al.*, Phys. Rev. C **47** (1993) 2502.
- 86) H. Mach *et al.*, Eur. Phys. J. A **25** (2005) 105.
- 87) C. M. Mattoon *et al.*, Phys. Rev. C **75** (2007) 017302.
- 88) M. Seidlitz *et al.*, Phys. Lett. **B700** (2011) 181.
- 89) J. R. Terry *et al.*, Phys. Rev. C **77** (2008) 014316.
- 90) D. Miller *et al.*, Phys. Rev. C **79** (2009) 054306.
- 91) T. Nakamura, *et al.*, Phys. Rev. Lett. **103** (2009) 262501.
- 92) M. Takechi *et al.*, Nucl. Phys. A **834** (2010) 412c.
- 93) M. Takechi *et al.*, Mod. Phys. Lett. A **25** (2010) 1878.
- 94) W. Horiuchi, Y. Suzuki, P. Capel, and D. Baye, Phys. Rev. C **81** (2010) 024606.
- 95) B. Jurado, *et al.*, Phys. Lett. **B649** (2007) 43.
- 96) K. Minomo, T. Sumi, M. Kimura, K. Ogata, Y. R. Shimizu and M. Yahiro, Phys. Rev. C **84** (2011) 034602.
- 97) K. Minomo, T. Sumi, M. Kimura, K. Ogata, Y. R. Shimizu and M. Yahiro, Phys. Rev. Lett., in print.
- 98) N. Furutachi, M. Kimura, A. Doté, Y. Kanada-En'yo and S. Oryu, Prog. Theor. Phys. **119** (2008) 403.
- 99) M. Milin *et al.*, Eur. Phys. J. A **41** (2009) 335.
- 100) W. von Oertzen *et al.*, Eur. Phys. J. A **43** (2010) 17.
- 101) W. von Oertzen *et al.*, Eur. Phys. J. A **46** (2010) 345.
- 102) G. Th. Kaschl *et al.*, Nucl. Phys. A **155** (1970) 417.
- 103) G. Mairle *et al.*, Nucl. Phys. A **363** (1981) 413.
- 104) Z. Elekes, *et al.*, Phys. Lett. **B599** (2004) 17.
- 105) C. E. Svensson *et al.*, Phys. Rev. C **63** (2001) 061301.
- 106) E. Ideguchi *et al.*, Phys. Rev. Lett. **87** (2001) 222501.
- 107) C. D. O'Leary *et al.*, Phys. Rev. C **61** (2001) 064314.
- 108) R. R. Rodriguez-Guzman, J. L. Egido, and L. M. Robledo, Phys. Rev. C **62** (2000) 054308.
- 109) T. Inakura *et al.*, Nucl. Phys. A **710** (2003) 261.
- 110) M. Bender, H. Flocard, and P.-H. Heenen, Phys. Rev. C **68** (2003) 044321.
- 111) M. P. Nicoli *et al.*, Phys. Rev. C **60** (1999) 064608.
- 112) W. von Oertzen, H. G. Bohlen, and D. T. Khoa, Nucl. Phys. A **722** (2003) 702.
- 113) S. Ohkubo and K. Yamashita, Phys. Rev. C **66** (2002) 021301(R).
- 114) M. Gai *et al.*, Phys. Rev. Lett. **47** (1981) 1878.
- 115) K. Morita *et al.*, Phys. Rev. Lett. **55** (1985) 185.
- 116) M. Kimura and H. Horiuchi, Phys. Rev. C **69** (2004) 051304(R).
- 117) W. J. Gerace and A. M. Green, Nucl. Phys. A **93** (1967) 110.
- 118) W. J. Gerace and A. M. Green, Nucl. Phys. A **123** (1969) 241.
- 119) T. Ogawa, Y. Suzuki and K. Ikeda, Prog. Theor. Phys. **57** (1977) 1072.
- 120) T. Sakuda and S. Ohkubo, Phys. Rev. C **49** (1994) 149.
- 121) T. Yamaya *et al.*, Phys. Lett. **B306** (1993) 1.
- 122) T. Yamaya *et al.*, Nucl. Phys. A **573** (1994) 154.
- 123) Y. Kanada-En'yo and M. Kimura, Phys. Rev. C **72** (2005) 064322.
- 124) Y. Taniguchi, M. Kimura, Y. Kanada-En'yo and H. Horiuchi, Phys. Rev. C **76** (2007) 044317.
- 125) Z. Elekes *et al.*, Phys. Lett. **B586** (2004) 34.
- 126) Y. Kanada-En'yo, Phys. Rev. C **71** (2005) 014310.
- 127) M. Takashina, Y. Kanada-En'yo and Y. Sakuragi, Phys. Rev. C **71** (2005) 054602.
- 128) H. J. Ong *et al.*, Phys. Rev. C **78** (2008) 014308.
- 129) Y. Kanada-En'yo and H. Horiuchi, Phys. Rev. C **55** (1997) 2860.
- 130) D. R. Tilley *et al.*, Nucl. Phys. A **745** (2004) 155.
- 131) Y. Kanada-En'yo, Phys. Rev. C **84**, 024317 (2011).
- 132) M. Honma, H. Sagawa Prog. Theor. Phys. **84** (1990) 494.
- 133) I. Hamamoto and H. Sagawa, Phys. Rev. C **53** (1996) R1492.
- 134) F. Catara, E. G. Lanza, M. A. Nagarajan and A. Vitturi, Nucl. Phys. A **624** (1997) 449.
- 135) G. Colo and P. F. Bortignon, Nucl. Phys. A **969** (2001) 427.

- 136) T. Nakatsukasa and K. Yabana, Phys. Rev. C **71** (2005) 024301.
- 137) T. Inakura, T. Nakatsukasa and K. Yabana, Phys. Rev. C **80** (2009) 044301.
- 138) Y. Kanada-En'yo and M. Kimura, Phys. Rev. C **72** (2005) 064301.
- 139) T. Furuta, K.H.O. Hasnaoui, F. Gulminelli, C. Leclercq, A. Ono, Phys. Rev. C **82** (2010) 034307.
- 140) J. Rizzo, M. Colonna and A. Ono Phys. Rev. C **76** (2007) 024611.
- 141) M. Colonna, A. Ono, J. Rizzo Phys. Rev. C **82** (2010) 054613.
- 142) M. Colonna *et al.*, Nucl. Phys. A **642** (1998) 449.
- 143) Ph. Chomaz, M. Colonna, J. Randrup, Phys. Rep. **389** (2004) 263.
- 144) J.D. Frankland, B. Borderie, M. Colonna *et al.*, Nucl. Phys. A **689** (2001) 940.
- 145) W. Reisdorf, Prog. Theor. Phys. Suppl. **140** (2000) 111.
- 146) H. Takemoto, H. Horiuchi and A. Ono, Phys. Rev. C **54** (1996) 266.
- 147) D.H.E. Gross, Phys. Rep. **279** (1997) 120.
- 148) D.H.E. Gross, Phys. Chem. Chem. Phys. **4** (2002) 863.
- 149) A. Ono and H. Horiuchi, Phys. Rev. C **53** (1996) 845.
- 150) A. Ono and H. Horiuchi, Phys. Rev. C **53** (1996) 2341.
- 151) A. Ohnishi and J. Randrup, Nucl. Phys. A **565** (1994) 474.
- 152) Y. Sugawa and H. Horiuchi, Phys. Rev. C **60** (1999) 064607.
- 153) J. Schnack and H. Feldmeier, Phys. Lett. **B409** (1997) 6.
- 154) Y. Sugawa and H. Horiuchi, Prog. Theor. Phys. **105** (2001) 131.
- 155) T. Furuta and A. Ono, Phys. Rev. C **74** (2006) 014612.
- 156) T. Furuta, A. Ono, Phys. Rev. C **79** (2009) 014608.
- 157) H. S. Xu *et al.*, Phys. Rev. Lett. **85** (2000) 716.
- 158) A. Ono, P. Danielewicz, W.A. Friedman, W.G. Lynch and M.B. Tsang, Phys. Rev. C **68** (2003) 051601(R).
- 159) A. Ono, P. Danielewicz, W.A. Friedman, W.G. Lynch and M.B. Tsang, Phys. Rev. C **70** (2004) 041604(R).
- 160) H. Feldmeier, T. Neff, R. Roth, and J. Schnack, Nucl. Phys. A **632** (1998) 61.
- 161) T. Neff and H. Feldmeier, Nucl. Phys. A **713** (2003) 311.
- 162) R. Roth, T. Neff and H. Feldmeier, Prog. Part. Nucl. Phys. **65** (2010) 50.